International Journal of Heat and Mass Transfer 242 (2025) 126830

Contents lists available at ScienceDirect

International Journal of Heat and Mass Transfer

journal homepage: www.elsevier.com/locate/ijhmt

Bubble nucleation site density, generation frequency and departure diameter in flow boiling of HFE-7100

Ali H. Al-Zaidi [a], Mohamed M. Mahmoud [b], Atanas Ivanov [c], Tassos G. Karayiannis [c,*]

[a] University of Misan, Al-Amarah, 62001, Iraq
[b] Faculty of Engineering, Zagazig University, Zagazig 44519, Egypt
[c] Department of Mechanical and Aerospace Engineering, Brunel University London, Uxbridge UB8 3PH, UK

ARTICLE INFO

Keywords:
Flow boiling
Nucleation site density
Bubble generation frequency
Bubble departure diameter
Correlations

ABSTRACT

Bubble nucleation and dynamics can play a significant role in the nucleate boiling mechanism during flow boiling. Understanding the behaviour of nucleating bubbles at different operating conditions can help identify the control parameters that should be included in proposed heat transfer models and correlations. This paper presents an experimental work on measurements of active nucleation site density, bubble generation frequency and departure diameter during flow boiling of refrigerant HFE-7100 in a microgap heat exchanger. The microgap heat exchanger had a heated flat surface of 20 mm width, 25 mm length and an adiabatic transparent cover located 1 mm above the heated surface. This allowed direct flow visualisation using a high-speed, high-resolution camera of a relatively large observation area. The effect of heat flux, mass flux and system pressure on the active nucleation site density and bubble dynamics (frequency and departure diameter) was examined. All experiments were carried out at inlet sub-cooling of 5 K, inlet pressure of 1 and 2 bar, mass flux of 100−200 kg/m^2 s and wall heat flux up to 84 kW/m^2. The experimental results were then compared with existing models and correlations predicting nucleation site density, bubble generation frequency and departure diameter with limited success. The dominant parameters were also identified, and new correlations were proposed based on the experimental results. The results of the current work can help develop accurate prediction heat transfer models and encourage and enable researchers working in numerical modelling to consider nucleation from multiple sites, rather than simulating one single nucleation site.

1. Introduction

Two-phase flow boiling in heat exchangers is an effective heat transfer mode in power, refrigeration and air conditioning systems and, at the small to micro scales, in cooling high-heat flux electronics. This is because high heat transfer rates can be dissipated from the heated surface with small changes in the boiling surface temperature. It is well-known that flow boiling can be classified into two main categories, sub-cooled and saturated flow boiling. In sub-cooled flow boiling, the liquid temperature outside the wall thermal boundary layer is below the saturation temperature and thus bubbles that nucleate, grow and depart from the heated surface, can then collapse in the liquid bulk due to condensation. Additionally, the bubble shape is flattened at the upper surface of the bubble due to condensation effects as reported by Zhou et al. [1]. On the contrary, in saturated flow boiling, the liquid temperature outside the wall thermal boundary layer equals the saturation temperature and thus bubbles do not condense and continue to grow with further developments in flow patterns from bubbly to annular flow. Additionally, the bubbles are nearly spherical in shape compared to the flattened shape in sub-cooled boiling. Therefore, the heat transfer mechanisms and modelling approach in saturated boiling is different compared to sub-cooled flow boiling. Furthermore, bubble characteristics can be affected by several factors, as reported by [2,3]. These include, in addition to the operating conditions, working fluid, surface characteristics, channel geometry and orientation.

Several models/correlations were proposed by a number of researchers working in flow boiling heat transfer studies either based on the contribution of convective and nucleate boiling mechanisms or fitting the data with dimensionless groups. An example is the commonly used superposition modelling approach given by Chen [4]. It is worth mentioning that in small to micro-scale applications there are large discrepancies among the existing models/correlations, despite the large number of proposed micro-scale models/correlations. Fang et al. [5]

* Corresponding author at: Department of Mechanical and Aerospace Engineering, Brunel University London, Uxbridge, Middlesex, UB8 3PH, UK.
E-mail address: tassos.karayiannis@brunel.ac.uk (T.G. Karayiannis).

https://doi.org/10.1016/j.ijheatmasstransfer.2025.126830
Received 23 November 2024; Received in revised form 10 January 2025; Accepted 13 February 2025
Available online 20 February 2025

Nomenclature

A	Area, [m^2]
B	Constant, [-]
Bo	Boiling number, [-], $Bo = q''_w/Gi_{lg}$
C	Constant, [-]
Co	Confinement number, [-], $Co = (\sigma/g\Delta\rho)^{0.5}/D_h$
cp	Specific heat capacity, [J/kg K]
C_{RB}	Empirical constant, [m/s$^{0.5}$]
D	Diameter, [m]
f	Frequency, [Hz]
f_{exp}	Experimental Fanning friction factor, [-]
G	Mass flux, [kg/m^2 s]
g	Gravitational acceleration, [m/s^2]
h	Heat transfer coefficient, [W/m^2 K]
$\bar{h}$	Average heat transfer coefficient, [W/m^2 K]
H	Height, [m]
i_{lg}	Latent heat of vaporization, [J/kg]
k	Thermal conductivity, [W/m K]
L	Length, [m]
Ja	Jackob number, [-], $Ja = \rho_l cp_l \Delta T_{sup}/\rho_g i_{lg}$
m	Constant, [-]
$\dot{m}$	Mass flow rate, [kg/s]
n	Active nucleation site, [-]
N	Number of data points, [-]
nu	Kinematic viscosity, [m^2/s]
$\overline{Nu}_{exp}$	Average experimental Nusselt number, [-]
P	Pressure, [Pa]
Pr_l	Prandtl number, [-], $Pr_l = cp_l\mu_l/k_l$
q''	Heat flux, [W/m^2]
R	Gas constant based on the molecular weight, [J/kg K]
Ra	Average surface roughness according to DIN ISO-4287:1997, [μm]
R_c	Cavity mouth radius, [m], $R_c = 2\sigma T_{sat}/\rho_g i_{lg}\Delta T_{sup}$
Re_l	Liquid Reynolds number, [-], $Re_l = GD_h/\mu_l$
Re_{ls}	Superficial liquid Reynolds number, [-], $Re_{ls} = GD_h(1-x)/\mu_l$
Rp	Maximum profile peak height according to DIN ISO-4287:1997, [μm]
RP	Reduced pressure, [-], $RP = P_{in}/P_{cr}$
s	Distribution parameter, [-]
Sa	Average surface roughness of scan area, [μm]
t	Time, [s]
T	Temperature, [K]
u_τ	Wall velocity, [m/s]
U	Absolute uncertainty, [-]
v	Specific volume, [m^3/kg]
W	Width, [m]
Y	Vertical distance between first row of thermocouples and gap surface, [m]
x	Vapour quality, [-]
z	Distance measured from channel inlet, [m]

Greek symbols

ΔP	Pressure drop, [Pa]
ΔT	Temperature difference, [K]
θ	Contact angle, [degree]
θ_t	Contact angle as a function of temperature, [degree]
θ_Y	Young's contact angle, [degree]
μ	Viscosity, [Pa s]
ρ	Density, [kg/m^3]
ρ^+	Non-dimensional density difference, [-]
σ	Surface tension, [N/m]
τ_w	Wall shear stress, [kg/m s^2]

Subscripts

b	Bubble, base
c	Viewing area
ch	Channel
cr	Critical
cu	Copper
d	Departure
exp	Experimental
g	Vapour, growth
h	Hydrolic
in	Inlet
l	Liquid
$meas$	Measured
$pred$	Predicted
sat	Saturated
sup	Superheat
sys	system
th	Thermocouple
w	Wall, waiting
z	Axial local

Abbreviations

MAE	Mean absolute error, [%]
NS	Nucleation site, [-]
NSD	Nucleation site density, [site/m^2]
ONB	Onset of nucleate boiling, [-]

assessed 50 models/correlations using a wide range of experimental data and found that few correlations gave reasonable prediction, e.g. five correlations out of the fifty predicted the data with MAE $<$ 40 %. The reasons for the discrepancies among the existing models/correlations were discussed by Karayiannis and Mahmoud [6] and [7]. In addition, the prediction of two-phase pressure drop is an additional challenge in the thermohydraulic design of small-scale cooling systems, as mentioned by Al-Zaidi et al. [8] who assessed a wide range of pressure drop models/correlations. Accordingly, the thermal design of two-phase small to micro heat exchangers is still hindered by the lack of general prediction models. This calls for further research in the bubble nucleation site density, departure diameter and frequency, which characterise the nucleate boiling region and affect the convective part that follows.

In general, in sub-cooled flow boiling at all heat exchanger sizes, the heat transfer mechanism is driven by bubble nucleation and agitation near the wall and single-phase forced convection. Thus, the heat transfer coefficient was predicted by calculating the wall heat flux using a commonly used approach called "the wall heat flux partitioning". This approach was suggested by Kurul and Podowski [9] and is commonly used in Computational Fluid Dynamics (CFD) commercial software packages with the name RPI (Rensselaer Polytechnic Institute). In the RPI heat flux model, the vapour bubble is assumed to lift-off from the nucleation site and enters the liquid bulk without slipping along the heated surface. This RPI model was modified by for example, Zhou et al. [1]. They observed that bubbles nucleate, slide along the heated surface then lift-off and thus they took the effect of bubble sliding and condensation into account. They reported that large portion of the superheated thermal boundary layer is removed by the bubbles during the sliding motion. This modelling approach depends on

Table 1
Models and correlations of bubble departure diameter.

Author(s)	Correlation	Fluid(s)
For pool boiling:		
Fritz [15]	$D_d = 0.0208\theta\sqrt{\frac{\sigma}{g\Delta\rho}}$ $\theta =$ 45° for water $\theta =$ 35° for refrigerants	Water & refrigerants
Cole and Rohsenow [16]	$D_d = CJa^{*5/4}\sqrt{\frac{\sigma}{g\Delta\rho}}$ $Ja^* = \frac{\rho_l cp_l T_{cr}}{\rho_g i_{lg}}$ $C =$ 0.00015 for water $C =$ 0.000465 for others	Water & refrigerants
Phan et al. [17]	$D_d = \left(6\sqrt{3/2}\right)^{1/3}\left(\frac{\rho_l}{\rho_g}\right)^{-0.5}\left(\frac{\rho_l}{\rho_g}-1\right)^{1/3}(tan\theta)^{-0.25}\sqrt{\frac{\sigma}{g\Delta\rho}}$	Water, n-pentane, FC-72 & HFE-7100
Cole [18]	$D_d = 0.04Ja\sqrt{\frac{\sigma}{g\Delta\rho}}$	Water, acetone, methanol & n-pentane
Kim and Kim [19]	$D_d = 0.1649Ja^{0.7}\sqrt{\frac{\sigma}{g\Delta\rho}}$	Water, methanol, n-pentane, R11, R113 & FC-72
For sub-cooled flow boiling:		
Kossolapov et al. [20]	$D_d = C_{RB}\sqrt{\frac{6nu_l}{u_\tau^2}}$ $u_\tau = \sqrt{\frac{\tau_w}{\rho_l}}$ $\tau_w = \frac{0.023Re^{-0.2}G^2}{\rho_l}$ $C_{RB} = B/2$ $B:$ theoretical constant, see Table 2 in their paper	Water
For saturated flow boiling:		
Lie and Lin [11]	$\frac{D_d}{\sqrt{\sigma/g\Delta\rho}} = 0.353(\rho_l/\rho_g)^{0.5}Re_{ls}^{-0.2}Bo^{0.2}Co^{0.19}$	R134a
Lie et al. [12]	$\frac{D_d}{\sqrt{\sigma/g\Delta\rho}} = 0.25(\rho_l/\rho_g)^{0.48}Bo^{0.21}Re_{ls}^{-0.08}$	FC-72
Hsieh et al. [13]	$\frac{D_d}{\sqrt{\sigma/g\Delta\rho}} = 0.9(\rho_l/\rho_g)^{0.5}Bo^{0.2}Re_{ls}^{-0.25}Co^{-0.2}$	R407C

sub-models/correlations for the prediction of bubble departure diameter, frequency, and nucleation site density (NSD), i.e. number of active nucleation sites per unit area. In other words, the accuracy of this method depends largely on the accuracy of the sub-models. Therefore, understanding the dependence of the NSD, departure diameter and frequency is important and can lead to improvements in the modelling/correlation attempts.

1.1. Bubble departure diameter and frequency

There are several models for the prediction of bubble departure diameter in pool boiling. Mahmoud and Karayiannis [10] presented a thorough analysis and discussion of pool boiling using three different fluids, namely water, HFE-7100 and FC-72. They evaluated a number of models and correlations of bubble departure diameter and reported large discrepancies. They found that one group of correlations predicted that the departure diameter was independent of wall-superheat, a second group that the departure diameter increased moderately with wall-superheat and a third group predicted that the departure diameter increased strongly with wall-superheat. They attributed this disagreement to the following reasons: (1) different thermal boundary conditions, i.e. constant surface temperature or constant heat flux, (2) different surface materials and microstructures, (3) measurement uncertainty in the bubble departure diameter, (4) definition of bubble diameter, i.e. equivalent diameter and (5) experimental methodology, i.e. increasing or decreasing heat flux. Other researchers, [11–13], studied saturated flow boiling of R134a, R407C and FC-72, and proposed correlations of bubble generation frequency and departure diameter. For example, Lie and Lin [11] investigated saturated flow boiling of R134a in a horizontal channel having 1 and 2 mm height. They performed their experiments at a system pressure of 4.14 and 4.88 bar, mass flux of 200–300 kg/m^2 s and heat flux up to 45 kW/m^2. Their results showed that the bubble departure diameter increased with increasing heat flux and decreasing mass flux and system pressure. The bubble frequency was found to increase with increasing heat flux, mass flux and system pressure. Thus, they correlated their data using the dimensionless groups, i.e. Reynolds number, boiling number and confinement number. Recently, Zhao et al. [14] studied sub-cooled flow boiling of water in a vertical annulus. They measured bubble dynamics at single and multiple nucleation sites using a high-speed camera. Their experiments were conducted at a system pressure of 1.5 bar, flow velocity of 0.5 m/s, inlet sub-cooling of 10–30 K and heat flux of 250–700 kW/m^2. Their results showed that the bubble departure diameter decreased with increasing heat flux and inlet sub-cooling. They attributed the reduction in departure diameter with heat flux to the method of conducting the experiments. In their tests, they controlled the local sub-cooling by varying the inlet sub-cooling with each heat flux value. In other words, two parameters were varied simultaneously, namely the heat flux and inlet sub-cooling. They reported that this could lead to a thinner superheated layer, i.e. high temperature gradient near the surface, and thus a reduction in the bubble departure diameter. The bubble frequency was found to increase with heat flux. They also found that, at low heat fluxes, the frequency decreased with increasing sub-cooling, while an opposite trend was found at high heat fluxes. They reported that both departure diameter and frequency have a stochastic nature, i.e. significant variation from site to site. Thus, they concluded that the models based on

Table 2
Models and correlations of bubble frequency.

Author(s)	Correlation	Fluid(s)
For pool boiling:		
Jakob and Fritz [21]	$f_b = \dfrac{0.078}{D_d}$	Water
Cole [22]	$f_b = \left(\dfrac{4g\Delta\rho}{3\rho_l}\right)^{0.5} / D_d{}^{0.5}$	Water, carbon tetrachloride, n-pentane, methanol & acetone
Zuber [23]	$f_b = \left(0.59\left(\dfrac{\sigma g\Delta\rho}{\rho_l{}^2}\right)^{0.25}\right) / D_d$	Water, carbon tetrachloride & methanol
For saturated flow boiling:		
Lie and Lin [11]	$\dfrac{f_b D_d}{\mu_l/(\rho_l D_h)} = 3.7 Re_{ls}{}^{1.33} Pr_l{}^2 Bo^{0.725} Co^{0.59}$	R134a
Lie et al. [12]	$\dfrac{f_b D_d}{\mu_l/(\rho_l D_h)} = 0.65 Re_{ls}{}^{1.3} Pr_l{}^{0.7} Bo^{0.66}$	FC-72
Hsieh et al. [13]	$\dfrac{f_b D_d}{\mu_l/(\rho_l D_h)} = 1.61 Re_{ls}{}^{1.4} Pr_l{}^2 Bo^{0.7} Co$	R407C

single-site measurements could be highly unreliable. Tables 1 and 2 summarize the models/correlations of bubble departure diameter and frequency proposed by researchers.

1.2. Nucleation site density

Nucleation site density was extensively studied in pool boiling, with water being the most frequently tested fluid, see Table 3. Most researchers reported that the NSD increased with heat flux or wall superheat and consequently they correlated their data using one of these two parameters, see [24] and [25]. Nucleation site density in saturated flow boiling was also investigated by [11–13]. The experimental study by [11] included R134a as a working fluid and found that the NSD increased with increasing heat flux and reducing mass flux. The effect of system pressure was found to be insignificant. They proposed a correlation by introducing the Reynolds number and Bond number. A number of researchers [26–30] carried out sub-cooled flow boiling studies using different working fluids such as water, R113 and R134a. Basu et al. [26] measured the nucleation site density in sub-cooled flow boiling of water using a high-speed camera on a copper surface with a contact angle of 30°. They allowed for cold water to flow into the system from another tank to overcome bubble coalescence at high heat fluxes, which can supress the bubble size and reduce the bubble merging. It was found that the nucleation site density was independent of mass flux and inlet sub-cooling, but it depended on the wall superheat. The NSD was found to increase either with increasing wall superheat or increasing contact

Table 3
Models and correlations of nucleation site density.

Author(s)	Correlation	Fluid(s)
For pool boiling:		
Gaertner and Westwater [24]	$NSD = q_w''^{\,2.1}$	Water
Lemmert and Chawla [25]	$NSD = (210\Delta T_{sup})^{1.805}$	Water
Wang and Dhir [31]	$NSD = 7.81\times10^{-29}(1-cos\theta)R_c^{-6}$	Water
Ardron and Giustini [32]	$NSD = BR_c^{-m}\left[erf\left(\dfrac{\theta_Y - 0.374}{s\sqrt{2}}\right) + erf\left(\dfrac{0.374}{s\sqrt{2}}\right)\right]$ $m = 3$ $B = 7\times10^{-12}/m$ $s = 0.285$ $\theta_Y = 0.133\left(\dfrac{T_w}{T_{cr}}\right)^{-9.95}$ T: temperature in degree absolute	Water
For sub-cooled flow boiling:		
Basu et al [26]	$NSD = 0.34\times10^4(1-cos\theta)(\Delta T_{sup})^2 \;\; (\Delta T_{sup,ONB} < \Delta T_{sup} < 15K)$ $NSD = 3.4\times10^{-1}(1-cos\theta)(\Delta T_{sup})^{5.3} \;\; (\Delta T_{sup} \geq 15K)$	Water
Yang et al. [27]	$NSD = 10^4(0.28\Delta T_{sup}{}^{2.66})$	Water
Lie and Lin [28]	$NSD = 80352 + 8034\Delta T_{sup}{}^{1.67} Co^{0.51}$	R134a
Li et al. [29]	$NSD = 10^3(1-cos\theta_t)\exp\{f(p)\}\Delta T_{sup}{}^{A\Delta T_{sup}+B}$ $f(p) = 26.006 - 3.678\exp(-2P) - 21.907 exp\left(-\dfrac{P}{24.065}\right)$ $A = -0.0002P^2 + 0.0108P + 0.0119$ $B = 0.122P + 1.988$ P is in MPa $1 - cos\theta_t = (1-cos\theta)\left(\dfrac{374 - T_{sat}}{374 - 25}\right)^{0.719}$	Applicable to Water
Hibiki and Ishii [30]	$NSD = 4.72\times10^5\left\{1 - exp\left(-\dfrac{\theta^2}{8\times0.722^2}\right)\right\}\left[\exp\left\{f(\rho^+)\dfrac{2.5\times10^{-6}}{R_c}\right\} - 1\right]$ $R_c = \dfrac{2\sigma\{1+(\rho_g/\rho_l)\}/P}{exp\,\{i_{lg}(T_w - T_{sat})/(RT_w T_{sat})\} - 1}$ $f(\rho^+) = -0.01064 + 0.48246\rho^+ - 0.22712\rho^{+2} + 0.05468\rho^{+3}$ $\rho^+ = log_{10}\left(\dfrac{\rho_l - \rho_g}{\rho_g}\right)$ P is in MPa	Evaluated data: Water & R113
For saturated flow boiling:		
Lie and Lin [11]	$NSD = \left[-0.029 + 4.82Bo^{0.409}Re_{ls}{}^{-0.15}\right]D_d{}^{-2}$	R134a
Lie et al. [12]	$NSD = \left[75Bo^{0.84}Re_{ls}{}^{-0.15}\right]D_d{}^{-2}$	FC-72
Hsieh et al. [13]	$NSD = \left[-0.009 + 1000Bo^{1.25}Re_{ls}{}^{0.05}Co^{0.06}\right]D_d{}^{-2}$	R407C

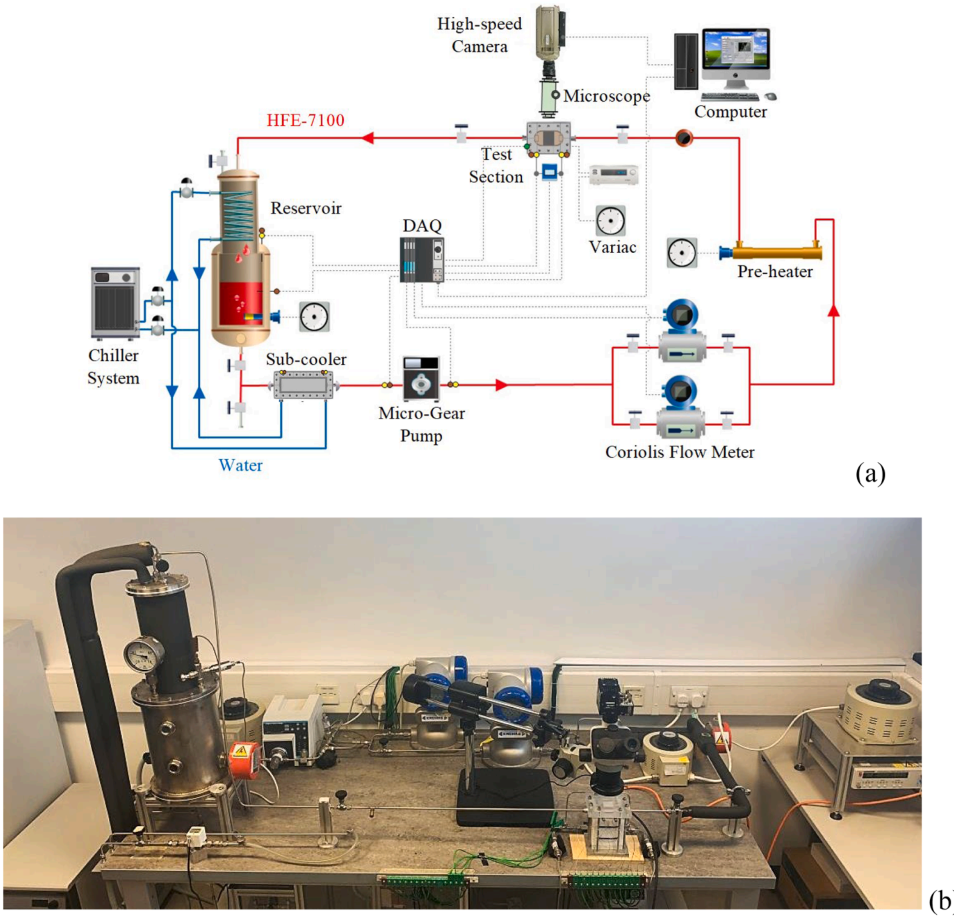

Fig. 1. Experimental facility: (a) Schematic diagram, [33] (b) Photograph.

angle. They compared their data with some existing correlations and found wide scatter. Thus, they proposed empirical correlations based on the wall superheat range, see Table 3, which summarizes the models/correlations of NSD suggested by researchers. They reported that their correlations were valid for other fluids and pressures as long as the wall superheat is above the superheat required for the onset of nucleate boiling. Zhao et al. [14] investigated sub-cooled flow boiling of water and showed that the nucleation site density increased with increasing heat flux, while the effect of inlet sub-cooling was insignificant.

As presented above, in most experimental studies, the nucleation site density was measured using water under highly sub-cooled conditions and the collected data were used to develop NSD models/correlations, which are widely used in literature. Additionally, there is a large number of micro-scale heat transfer models/correlations in literature but with large discrepancies. This discrepancy could arise from the accuracy of the sub-models adopted in these models/correlations for the nucleation site density, bubble departure diameter and frequency, which calls for more research. Thus, in the current study, active nucleation site density, bubble departure diameter and frequency were measured in flow boiling of HFE-7100 in a microgap at 5 K inlet sub-cooling. These parameters were not measured before in the past literature for this fluid, which is one of the recommended new generation coolants for electronic devices. The effect of heat flux, mass flux and system pressure were investigated. The collected experimental data were presented, discussed and used to evaluate existing models/correlations for the prediction of bubble departure diameter and frequency and NSD. The results of the current study will contribute to the development of accurate heat transfer models/correlations that are required for the design of flow boiling systems, including small to micro scale heat sinks operating in two-phase for cooling electronics. Additionally, it will help researchers working in numerical modelling include nucleation from multiple nucleation sites rather than one single nucleation site in their studies.

2. Experimental system and procedure

2.1. Experimental facility

Fig. 1 (a) shows the schematic diagram of the experimental system, while Fig. 1 (b) shows a photograph of the system. HFE-7100 was used as the test fluid, and it was stored in a reservoir, which included a cooling coil (helical copper tube) at the topside and an immersion heater inside the liquid. The coil, which was used as a condenser, was cooled using a circulation chiller. This coil along with the immersion heater was used to degas the test fluid before conducting the experiments and to control the system pressure during the experiments. A set of thermocouples and pressure transducers were also connected to the liquid reservoir. A plate heat exchanger (sub-cooler) was mounted between the reservoir and the pump to control the fluid inlet temperature before the pump suction. This sub-cooler is necessary to prevent pump cavitation. A micro gear-pump (Cole-Parmer with maximum flow rate of 2300 mL/min) with a digital driver was used to produce the required flow rate. Two thermocouples and two pressure transducers were placed at the pump suction and discharge. Two Coriolis flow meters (KROHNE Optimass) for low and high mass flow rates were connected to the experimental rig to measure the experimental flow rate. An electric preheater (FIREBAR) with 1.5 kW heating capacity was placed between these flow meters and the test section to control the fluid inlet temperature, i.e. inlet sub-cooling. The circulation chiller (Cole-Parmer Polystat chiller using glycol-water) had a cooling capacity of 2.9 kW. Three variable autotransformers (Carroll & Meynell) were used to control the

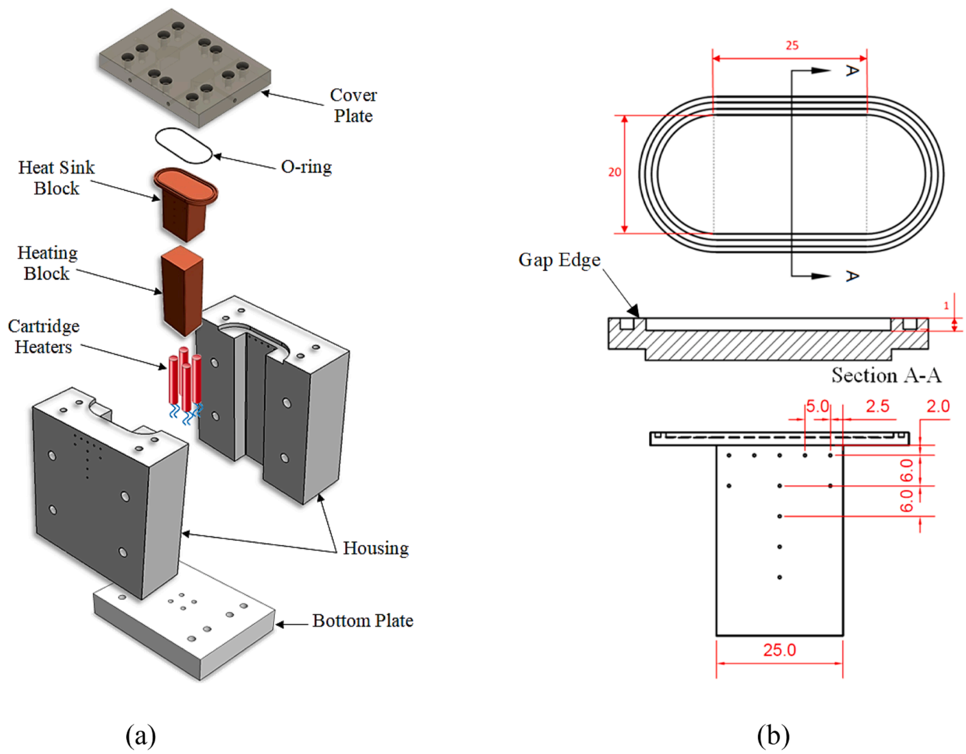

Fig. 2. Experimental test section: (a) Exploded drawing (b) Heat sink block (microgap) dimensions, in [mm].

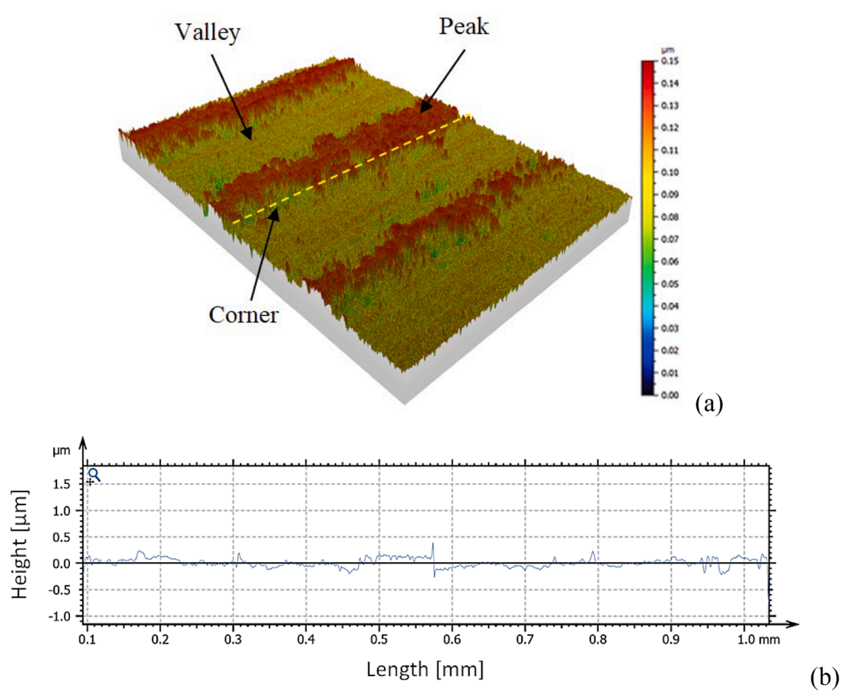

Fig. 3. Surface topography: (a) 3D scan area showing cutting marks as peaks and valleys (b) Profile line (The corner identified above is the edge between the end of the valley and the start of the peak).

supplied voltage then the input heat into the liquid reservoir, the pre-heater and the test section. A power meter (Hameg HM8115–2) with ±0.4 % accuracy was connected between a variable transformer and the test section to measure the input power. All the measuring instruments, such as thermocouples, pressure transducers and flow meters, were connected to the data acquisition system (DAQ) from National Instruments with a logging frequency of 1 kHz. The DAQ was then connected to a computer, and LabView software was used to save all the measured data. The visualization system consisted of the microscope (Huvitz) clamped on the LED lighting system. A high-speed, high-resolution, camera (Phantom Miro-C210) was then mounted on the topside of the microscope. This camera was set at 1800 fps and 1280 × 1024 pixel resolution to capture flow behaviour inside the test section.

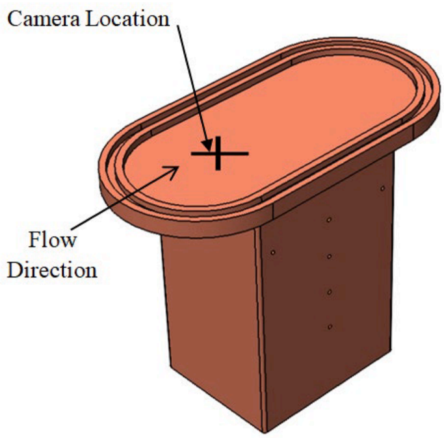

Fig. 4. Visualization location of present camera.

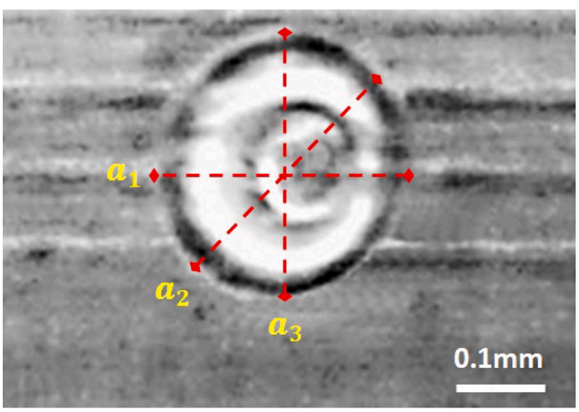

Fig. 5. Bubble size measurements.

2.2. Microgap test section

The test section assembly consisted of six main parts namely bottom plate, housing, cartridge heaters, heater block, heat sink block and cover plate as shown in Fig. 2 (a). A PTFE sheet was used to manufacture the bottom plate and the housing to minimize the heat loss during the experiments. The housing was designed as two parts and had 16 horizontal holes drilled to insert thermocouples. Four cartridge heaters with a total power of 700 W were inserted vertically into the heater block. These heaters were used to supply the required heating power to the test section. Both the heater block and the heat sink block were made of oxygen-free copper. They were clamped together and a thermal paste (RS 503–357) was applied between them. In addition, an O-ring was inserted between the heat sink block and the cover plate to prevent any leakage. A transparent polycarbonate sheet was used to manufacture the cover plate in order to allow flow visualization. The cover plate included two semi-circular manifolds and six tapping holes to connect the inlet/outlet flow tubes, inlet/outlet fluid thermocouples and inlet/outlet fluid pressure transducers. Two T-type thermocouples and connections of two Omega pressure transducers were inserted into the cover plate to measure inlet/outlet fluid temperatures and pressures. In addition, one Omega differential pressure transducer with an accuracy of ±0.08 % was used to measure the total pressure drop inside the test section. A set of long bolts were inserted vertically around the test section to hold all these parts together. A high-precision micro-milling machine (HERMLE-C20U) was used to fabricate the heat sink block. Fig. 2 (b) shows the dimensions of the heat sink block that consisted of an O-ring groove and the microgap that were placed on the topside. The inlet and outlet plena had a semi-circular shape. The liquid enters the test section horizontally through a stainless-steel tube of 6.35 mm internal diameter. There is a change of direction at the wall of the plenum to enter the plenum vertically and subsequently change direction to flow horizontally in the plenum to the microgap. There is only one single channel (the microgap) and the size of the inlet plenum was large enough (much larger than the inlet pipe diameter) and ends with a cross section of the same dimensions at the microgap entry point, which results in no flow maldistribution. This design was also tested successfully with multi-microchannels and with CFD analysis for single-phase flow. Additional explanation and validation can be found in Al-Zaidi et al. [33]. Sixteen holes were drilled horizontally inside this block to insert K-type thermocouples. Readings from these thermocouples were used to calculate the supplied base heat flux to the test section, see Section 2.3. Five of these thermocouples were located horizontally along the heated length, with a vertical distance of 3.5 mm from the microgap bottom surface, with the readings used to calculate the local wall temperature of the bottom surface, see Section 2.3. The microgap height, width and length were 1, 20 and 25 mm, respectively. These dimensions were measured using an optical machine (ZEISS O-INSPECT) with an accuracy of ±0.002 mm.

The roughness of the microgap bottom surface was measured at three different locations and then the average value was taken. A 3D-Surface Metrology System (NP FLEX) was used in this analysis. All the surface data were then implemented in the Smile View Map software to generate 3D images and further examine the surface topography. Fig. 3 depicts the profile line and the 3D scan area of one location. The cutting marks can clearly be seen on this surface as shown in Fig. 3 (a). These marks were formed as grooves having peaks and valleys. Generally, the average surface roughness of the profile line *Ra* was found to be 0.12 μm at a cut-off value of 0.8 mm according to ISO-4288 [34]. The maximum profile peak height *Rp* was also measured and found to be 0.16 μm. In addition, the average surface roughness of the scan area *Sa* was 0.13 μm. It is worth mentioning that the average surface roughness *Sa* is better than *Ra* to present the surface topography since it covers the entire scan surface.

2.3. Experimental procedure and data analysis

A degassing process was first carried out to ensure pure fluid in the system. Both adiabatic and diabatic experiments were then conducted before two-phase flow experiments. This initial step is necessary to validate the experimental system and all measuring instruments. In the adiabatic process, the inlet fluid conditions were set at 1 bar and nearly 23 °C, while the mass flow rate was increased gradually. The same procedure was carried out in the diabatic process, while supplying heat to the test section.

The two-phase experiments were carried out at different operating conditions. The system pressure, i.e. the inlet pressure at the test section, was set at 1 and 2 bar. The inlet sub-cooling was kept at about 5 K, while the mass flux and the wall heat flux were varied between 100−200 kg/m^2 s and up to 84 kW/m^2, respectively. The wall and base heat flux calculation procedure is presented below. The exit vapour quality corresponding to these conditions was up to 0.13. It is worth mentioning that the heat flux was increased further during the experiments till the exit quality of one or CHF was reached. However, only the results up to 84 kW/m^2 were presented in this study, i.e. before the onset of bubble coalescence. The supplied heat flux was controlled by the variable transformer and increased step by step. LabView software was adopted to save all measured signals and monitor any fluctuations in these signals. The data were saved for two minutes after a small variation with the time in the temperatures, pressures and flow rates was reached, i.e. less than 5 %. The data were then averaged over the two-minute interval to be used in the calculations. The Engineering Equation Solver (EES) software was used to obtain all fluid thermophysical properties and calculate the output variables.

The flow patterns were captured using a high-speed, high-resolution

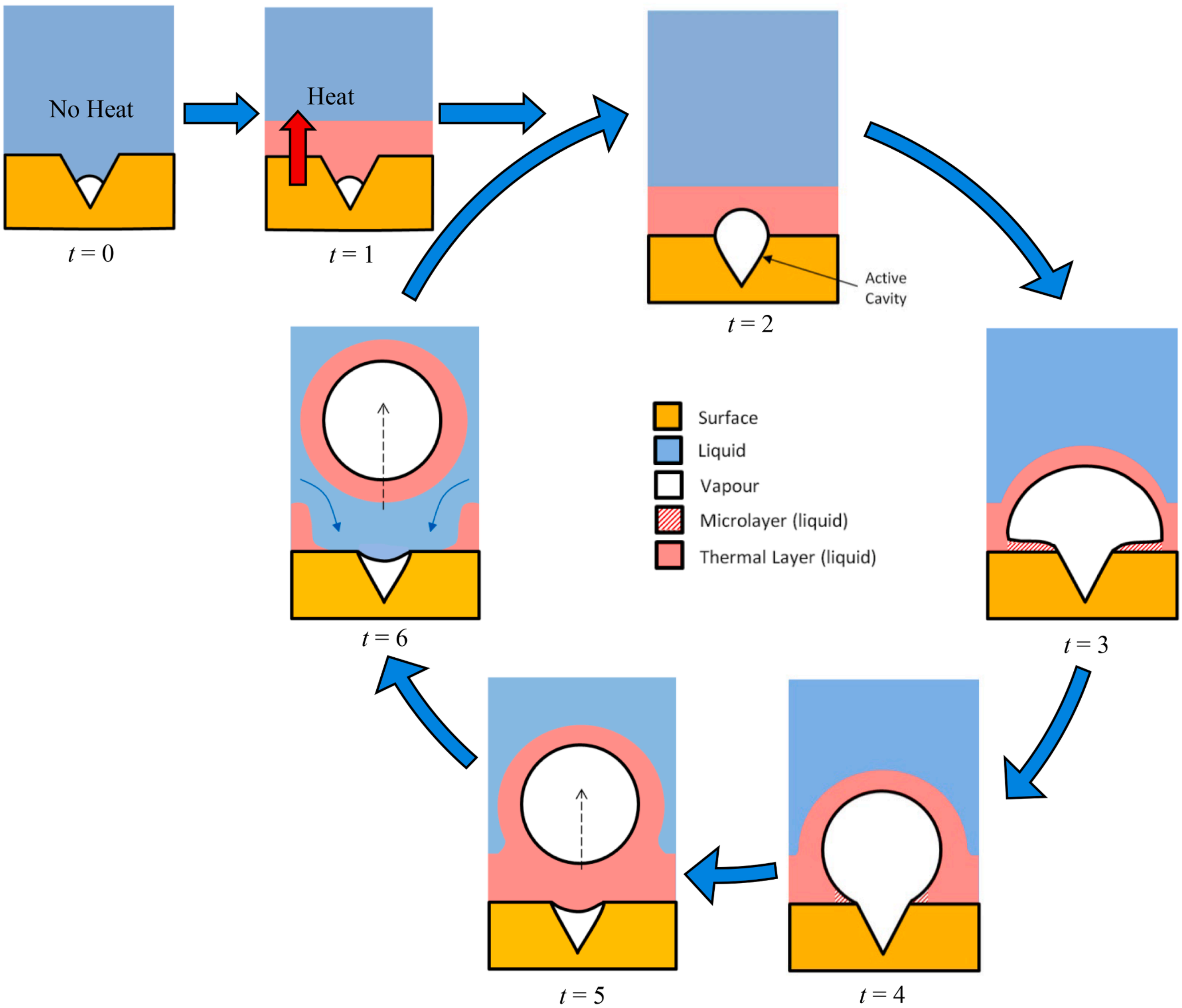

Fig. 6. Schematic of bubble growth cycle.

Table 4
Experimental uncertainty.

Variables	Uncertainty
Temperature (T-type)	±0.22 K
Temperature (K-type)	±0.21–0.6 K
Pressure (inlet transducer)	±0.25 %
Pressure (outlet transducer)	±0.22 %
Differential pressure	±0.07 %
Coriolis mass flow rate	±0.035 %
Fanning friction factor	±12–13 %
Average Nusselt number	±9–14.5 %
Mass flux	±0.2 %
Reynolds number	±5 %
Wall heat flux	±1.5–15 %
Nucleation site density	±10 %
Bubble departure diameter	±5.5–19 %
Bubble frequency	±10–23 %

Phantom camera and Phantom Camera Control software (PCC). The camera was located near the inlet and in the saturated flow region to clearly capture nucleating bubbles, see Fig. 4. The PCC software was also used to convert the recorded videos to a sequence of pictures to measure bubble dynamics. These videos were also played frame by frame to track flow features. The active nucleation site density was computed by dividing the total number of active nucleation sites n by the viewing area A_c of 8.8 mm × 11 mm, as in Eq. (1) below.

$$NSD = \frac{n}{A_c} \tag{1}$$

The number of active nucleation sites was counted manually. These sites on the surface can be easily counted at low heat fluxes. However, the coalescence rate increased with increasing heat flux resulting in merged bubbles. Therefore, it was difficult to accurately measure bubble characteristics at high heat fluxes, i.e. greater than 84 kW/m^2. Further details are presented in Section 3.2.

The camera lens was fixed at a constant focal-length, i.e. fixed viewing area, to reduce any errors in calibration. The camera was carefully calibrated using the horizontal gap edge, i.e. 1 mm, as a reference scale, see Fig. 2 (b). The width of this edge was first measured using a micrometre with an accuracy of ±1 μm. The calibration conversion from pixel size to distance unit was then found using the PCC software. The pixel size was converted to μm by multiplying by this conversion parameter in order to measure the bubble departure diameter. The bubble departure diameter was measured after the bubbles left their nucleation sites. This was carried out by taking the mean value of

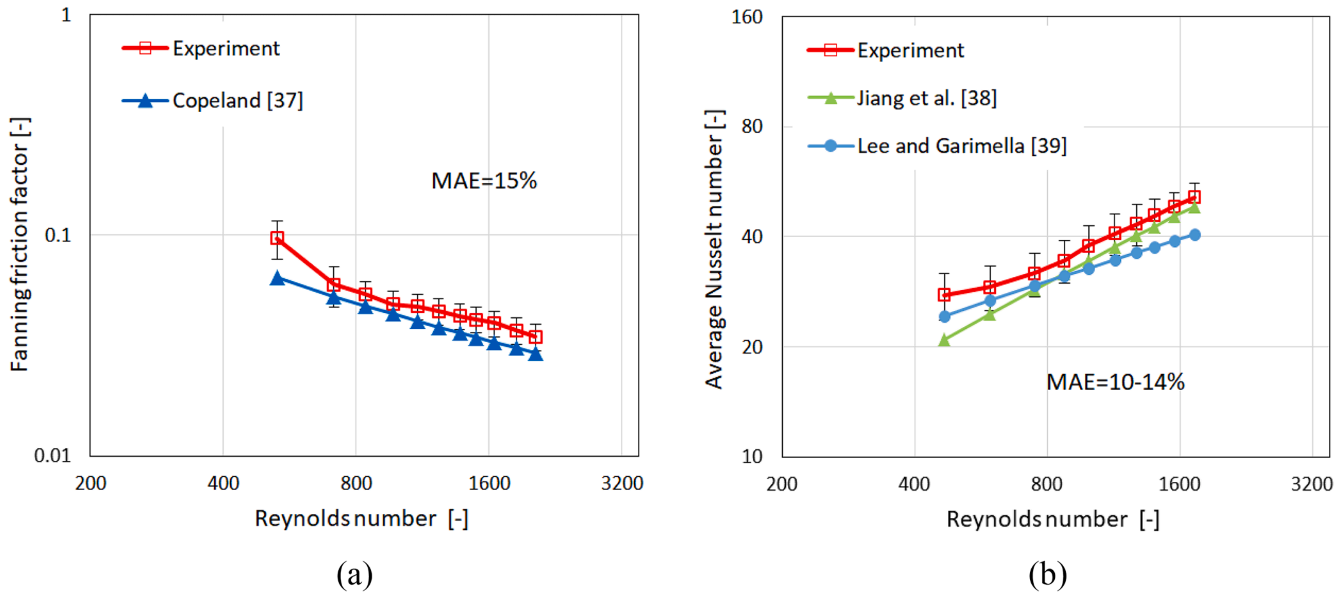

Fig. 7. Single-phase validation: (a) Adiabatic process (b) Diabatic process.

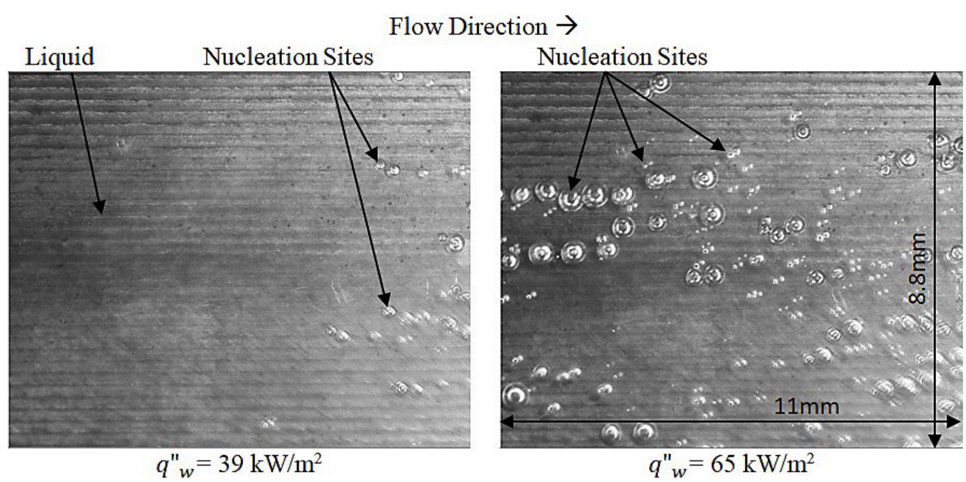

Fig. 8. Effect of heat flux on the nucleation site density at P_{sys}=1 bar and G=100 kg/m^2 s.

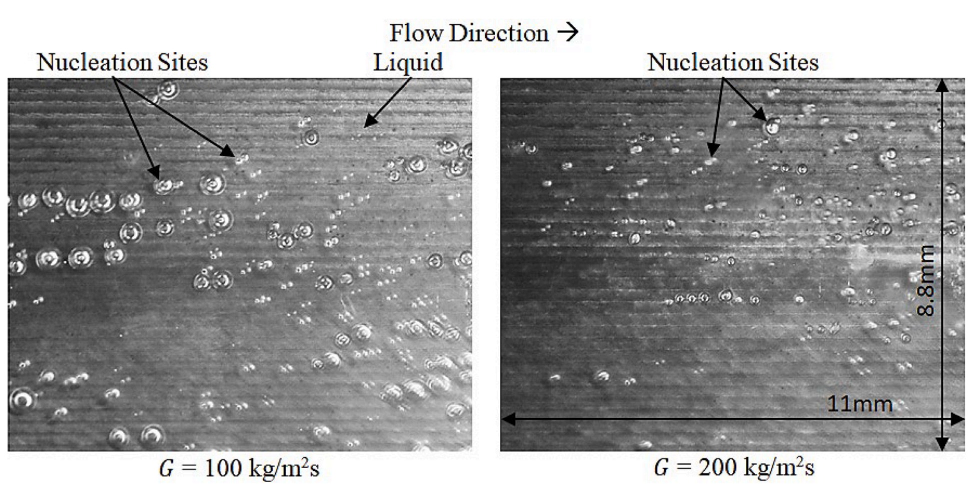

Fig. 9. Effect of mass flux on the nucleation site density at P_{sys}= 1 bar and q''_w= 65 kW/m^2.

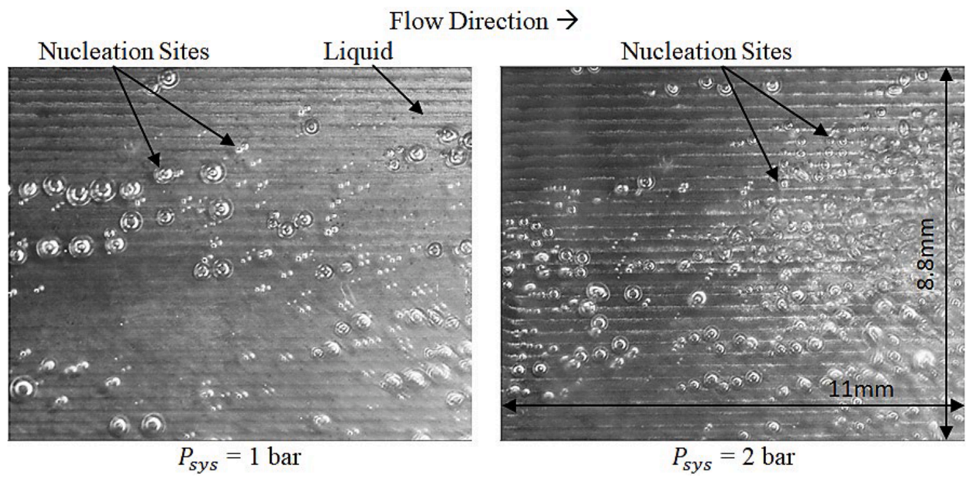

Fig. 10. Effect of system pressure on the nucleation site density at G= 100 kg/m^2 s and q''_w= 65 kW/m^2.

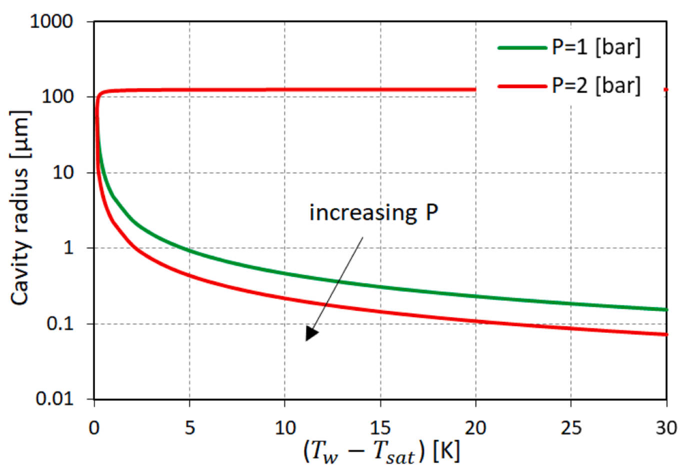

Fig. 11. Range of active surface cavities at different system pressures using Hsu's model [40].

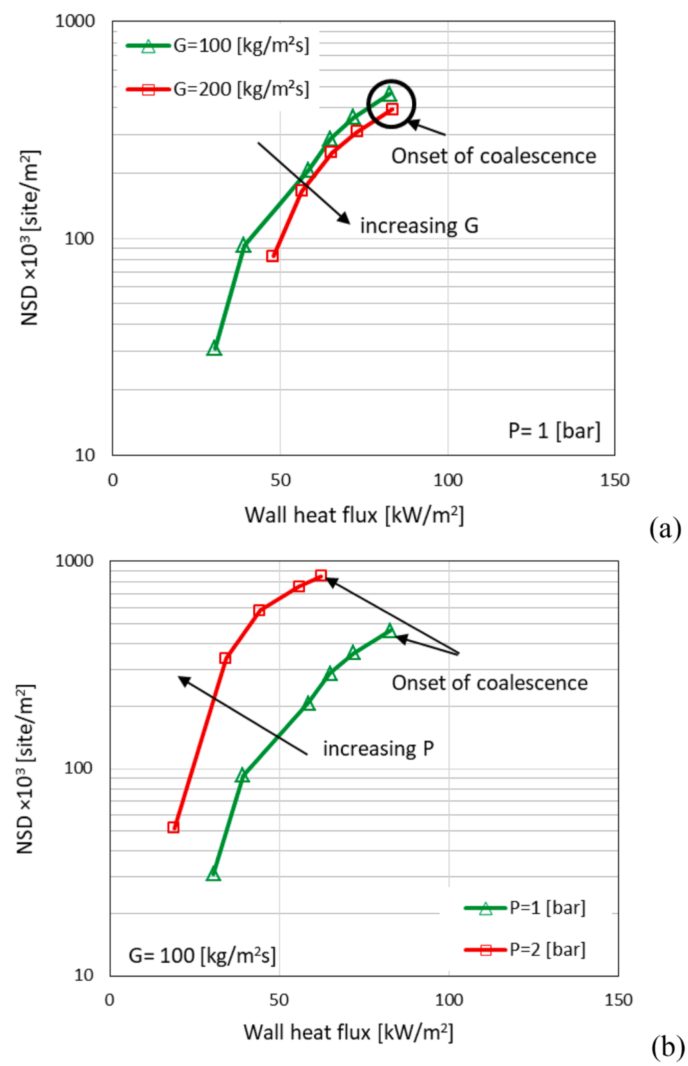

Fig. 12. Effect of heat flux, mass flux and system pressure on the nucleation site density.

the axial (a1), diagonal (a2) and transverse (a3) dimensions of each single departing bubble, as shown in Fig. 5. After that, the average value of all bubbles, seen in the capture area of 8.8 mm × 11 mm, was taken to present the average bubble departure diameter D_d. The growth time t_g and the waiting time t_w were measured for each single bubble, and then the average values were taken. The growth time is the time that the bubble spends on the hot surface to grow, i.e. (t = 1–t = 5), see the schematic in Fig. 6. Once this bubble departs the surface, a new bubble will form on the same site. This period between the departing bubble and new one is called the bubble waiting time, i.e. (t = 6–t = 2). The bubble waiting time is also defined as the required time to reform the wall thermal boundary layer, which is disrupted when the nucleating bubble leaves the nucleation site. The summation of these two times was then used to calculate the bubble generation frequency as follows:

$$f_b = 1/(t_g + t_w) \quad (2)$$

The bubble frequency represents the number of nucleating bubbles that are generated by one site per second. The average value of the bubble generation frequency was obtained by taking the average frequency for all the bubbles recorded in the 8.8 mm × 11 mm view area.

As mentioned above, the experimental facility was validated using single-phase flow and heat transfer experiments. The data reduction used in the single-phase validation is summarised as follows:

The experimental fanning friction factor was calculated from Eq. (3).

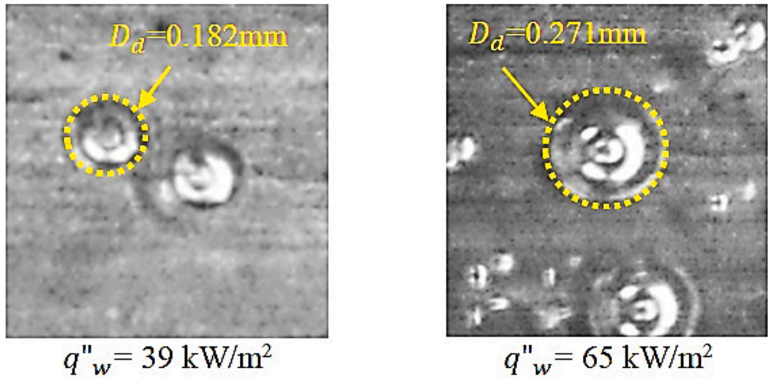

Fig. 13. Effect of heat flux on the bubble departure diameter at P_{sys}= 1 bar and G= 100 kg/m^2 s.

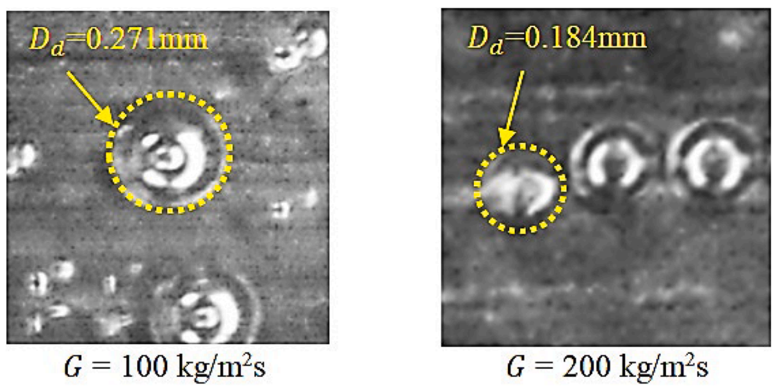

Fig. 14. Effect of mass flux on the bubble departure diameter at P_{sys}= 1 bar and q''_w= 65 kW/m^2.

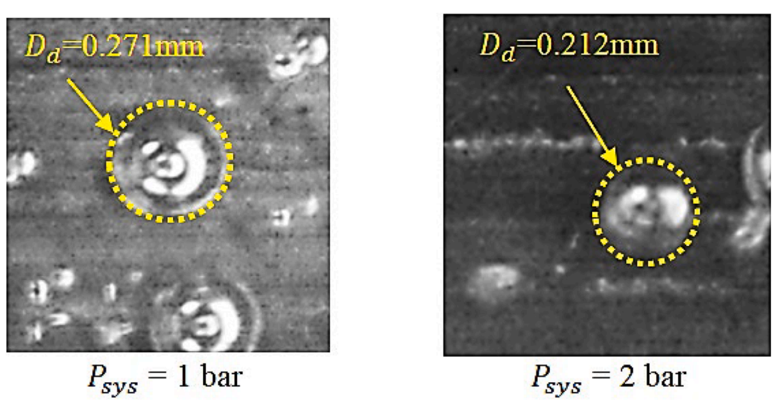

Fig. 15. Effect of system pressure on the bubble departure diameter at G= 100 kg/m^2 s and q''_w= 65 kW/m^2.

$$f_{exp} = \frac{\Delta P_{meas} D_h}{2 L_{ch} v_l G^2} \tag{3}$$

The pressure drop ΔP_{meas} was measured directly from the differential pressure transducer. The hydraulic diameter D_h was found from Eq. (4), while the mass flux was calculated using Eq. (5).

$$D_h = \frac{2 H_{ch} W_{ch}}{H_{ch} + W_{ch}} \tag{4}$$

$$G = \frac{\dot{m}}{H_{ch} W_{ch}} \tag{5}$$

L_{ch} is the 20 mm channel length. Eq. (6) was used to calculate the average Nusselt number as follows:

$$\overline{Nu}_{exp} = \frac{\bar{h} D_h}{k_l} \tag{6}$$

The average heat transfer coefficient $\bar{h}$ was calculated from Eq. (7), while the local heat transfer coefficient $h_{(z)}$ was found at five locations along the heated length using Eq. (8).

$$\bar{h} = \frac{1}{L_{ch}} \int_0^{L_{ch}} h_{(z)} dz \tag{7}$$

$$h_{(z)} = \frac{q''_w}{(T_{w(z)} - T_{l(z)})} \tag{8}$$

Eq. (9) was used to calculate the local wall temperature $T_{w(z)}$, while

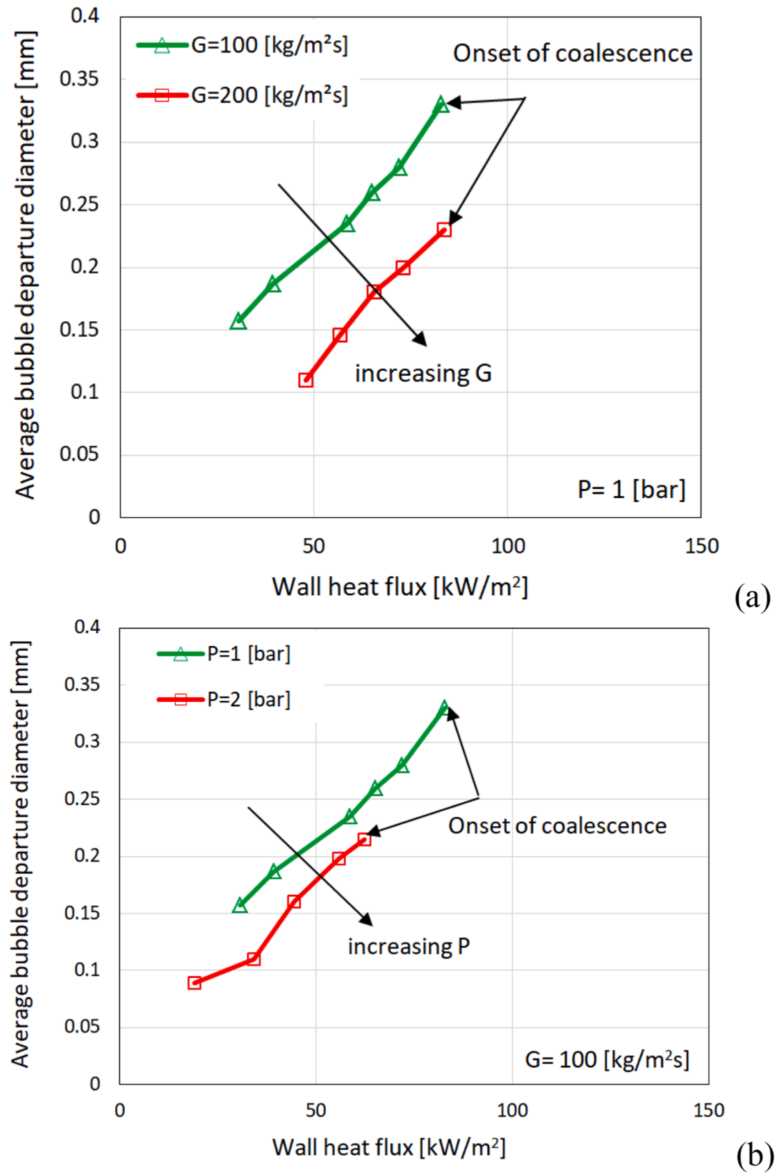

Fig. 16. Effect of heat flux, mass flux and system pressure on the average bubble departure diameter.

Eq. (10) was used to find the local liquid temperature $T_{l(z)}$.

$$T_{w(z)} = T_{th(z)} - \frac{q_b'' Y}{k_{cu}} \tag{9}$$

$$T_{l(z)} = T_{l,in} + \frac{q_b'' W_{ch} z}{\dot{m} cp_l} \tag{10}$$

$T_{th(z)}$, $T_{l,in}$, z and Y are the local temperature along the heated length obtained from the thermocouples, the liquid inlet temperature, the local distance from the channel inlet and the vertical distance between the first row of thermocouples and the gap surface (3.5 mm), respectively. A best-fit linear equation was obtained using readings from the five thermocouples and corresponding locations in the heater block, see Fig. 2 (b). This expression was then differentiated to obtain the temperature gradient with distance from the microgap surface and hence the base heat flux from Eq. (11) below.

$$q_b'' = k_{cu} \frac{dT}{dy}\bigg|_{y=0} \tag{11}$$

The heat transfer active surface includes the base of the microgap, $W_{ch} \times L_{ch}$ plus the two side walls of surface area $H_{ch} \times L_{ch}$. The wall heat flux can then be obtained from the base heat flux values using Eq. (12) below.

$$q_w'' = \frac{q_b'' W_{ch}}{(2H_{ch} + W_{ch})} \tag{12}$$

Further details are also available in Al-Zaidi [33]. The liquid Reynolds number can be calculated using Eq. (13).

$$Re_l = \frac{G D_h}{\mu_l} \tag{13}$$

where μ_l is the liquid viscosity.

2.4. Uncertainty analysis

Table 4 presents the experimental uncertainties of all variables. The uncertainties in the measured variables (temperature, pressure and mass flow rate) were found from the calibration process or the datasheet by the manufacturer. A precision thermometer (ASL-F250 MK II) and a constant temperature bath using water-glycol were used to calibrate all

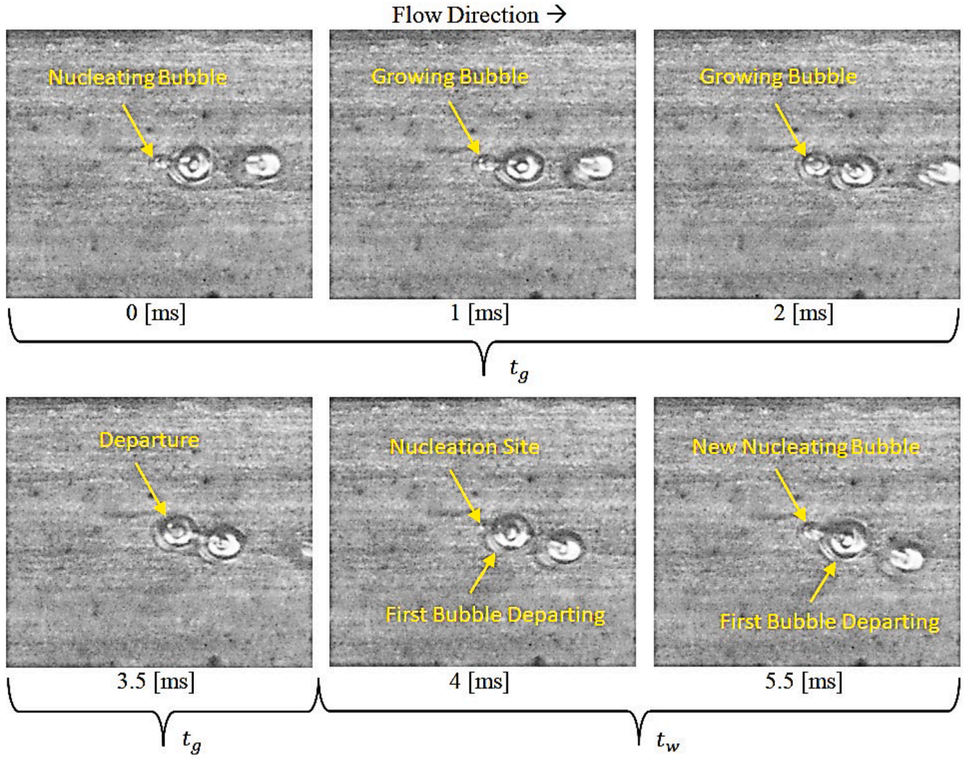

Fig. 17. Sequence of images of bubble ebullition cycle at P_{sys} = 1 bar, q''_w = 39 kW/m^2 and G = 100 kg/m^2 s. (t_g: Growth time, t_w: Waiting time).

thermocouples. The uncertainties in the calculated variables (Fanning friction factor, average Nusselt number, wall heat flux, mass flux, nucleation site density, bubble departure diameter and bubble frequency) were derived based on the method described by Coleman and Steele [35].

The uncertainty in NSD measurements could result from the accuracy of both n and A_c. The uncertainty of the viewing area A_c can be derived from the viewing length and width, after the pixel size was converted to μm using the calibration conversion. The uncertainty in the total number of active nucleation sites n was due to the random errors since these sites were counted manually for each frame of the images captured by the high-speed camera. These manual counts were conducted twice for the same set of images in order to reduce the uncertainty in n. It was found that, at high wall superheat (before the onset of coalescence), i.e. high number of nucleation sites, the difference between these two counts was only 2−3 sites for a total number of sites ranging from 45 to 82. As discussed above, the pixel size was multiplied by the calibration conversion to convert it to μm unit, and then to measure the bubble departure diameter. Therefore, the uncertainty in this measurement could result from the accuracy of the calibration conversion and the image measurement. The accuracy of the pixel measurement was taken to be ±2 pixel, see [36] for more details. The uncertainty of the bubble frequency was due to the uncertainties in the measurement of bubble growth time and waiting time. These uncertainties in t_g and t_w could be as large as the interval time between two image frames. For the present camera settings, this interval time was only 0.5 ms. Therefore, this accuracy of ±0.5 ms was used for each time to derive the uncertainty of the bubble frequency. The equations used to calculate the uncertainty in the derived variables are included in Appendix A.

3. Results and discussion

3.1. Single-phase validation

System validation was performed using single-phase experiments before conducting the two-phase experiments. Fig. 7 (a) shows the experimental single-phase Fanning friction factor, while Fig. 7 (b) shows the single-phase Nusselt number plotted versus Reynolds number. The experimental results were compared with correlations proposed for laminar flow in non-circular channels. The figure demonstrates that there was a good agreement between the experimental data and these correlations. For example, the correlation by Copeland [37] predicted the experimental Fanning friction data with a mean absolute error of 15 %. The experimental data points of Nusselt number were predicted very well by the correlations of Jiang et al. [38] and Lee and Garimella [39] with a MAE of 10 % and 14 %, respectively.

3.2. Nucleation site density

Fig. 8 shows the pictures captured by the high-speed camera at 1 bar system pressure and 100 kg/m^2 s mass flux for two different values of heat flux, 39 and 65 kW/m^2. It is interesting to note that the nucleating bubbles were found to form first at the surface cutting marks. These marks with peak and valley shapes can help trigger boiling since the corners of these valleys could act as nucleating sites, see Fig. 3 (a). The figure shows that the nucleation site density was low at 39 kW/m^2 compared to 65 kW/m^2, i.e. the NSD increased with increasing heat flux and subsequent increase in wall temperature.

Fig. 9 depicts that, the NSD decreased as the mass flux increased from 100 to 200 kg/m^2 s for a fixed heat flux of 65 kW/m^2. An increase in mass flux (high inertia force) leads to a reduction in the thickness of the wall thermal boundary layer, which may result in a suppression of bubble nucleation and then subsequently smaller NSD.

Fig. 10 shows the effect of system pressure on the NSD at a mass flux of 100 kg/m^2 s and wall heat flux of 65 kW/m^2. It was observed that

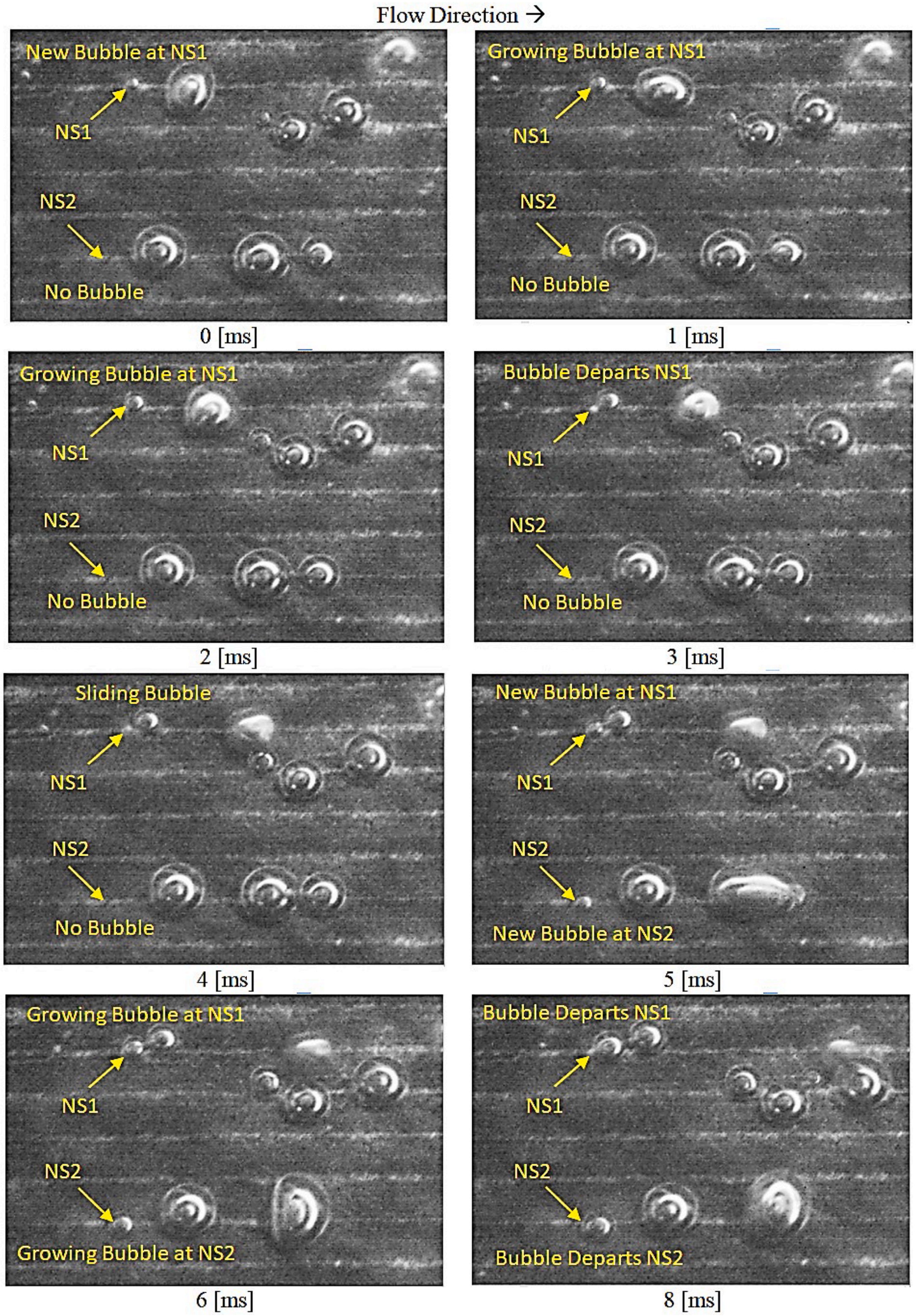

Fig. 18. Sequence of images of bubble ebullition cycle at two locations at P_{sys}= 1 bar, q''_w= 57 kW/m^2 and G= 200 kg/m^2 s (NS: Nucleation site).

when the system pressure increased from 1 bar to 2 bar, the NSD increased. It is well-known that surface tension decreases with increasing system pressure, which increases the size range of active nucleation sites as predicted by the Hsu model [40], see Fig. 11 for the two pressure values of this study. Therefore, increasing system pressure leads to the activation of the smaller surface cavities, i.e. more nucleation sites. Furthermore lower surface tension (higher pressure) leads to smaller bubble departure diameter (discussed later in Section 3.3). The net result is a higher number of nucleating bubbles that can be captured by the camera on the same heated area.

The effect of heat flux, mass flux and system pressure on the nucleation site density at different operating conditions is plotted in Fig. 12. The figure was plotted for wall heat fluxes up to 60−84 kW/m^2, where there was no bubble coalescence. With further increase in heat flux,

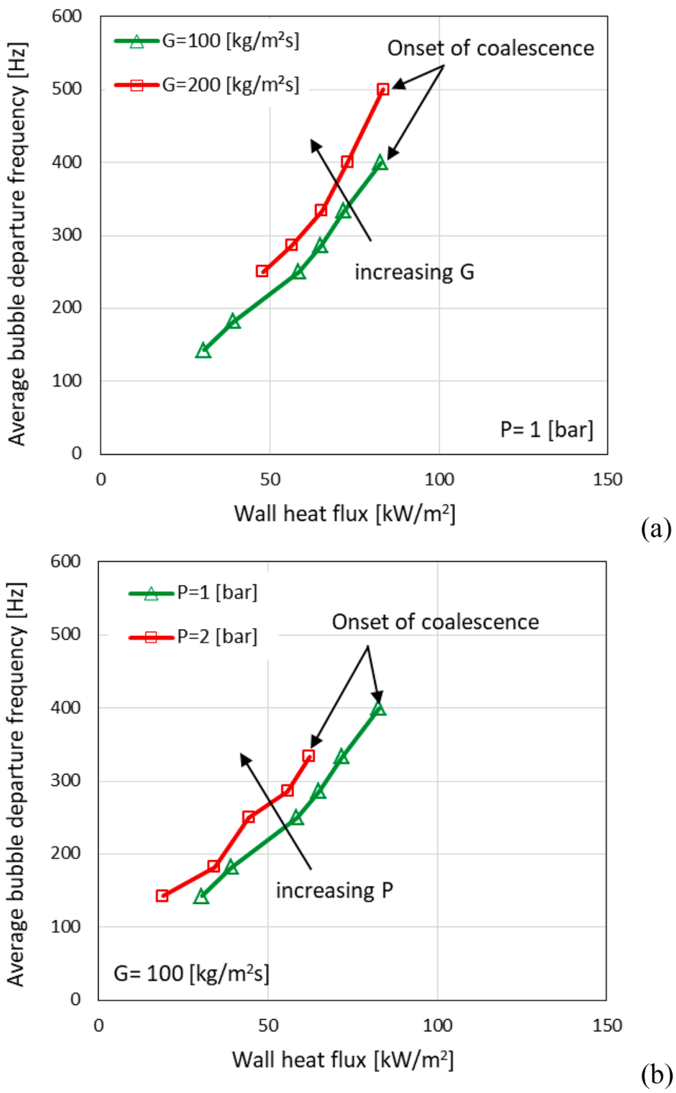

Fig. 19. Effect of heat flux, mass flux and system pressure on the average bubble frequency.

bubble coalescence occurred, and it was difficult to measure the NSD. It is clear that the NSD increased with increasing wall heat flux, system pressure and reducing mass flux. However, the effect of mass flux was found to be small.

3.3. Average bubble departure diameter

Figs. 13–15 show pictures obtained with the high-speed high-resolution camera of bubble departure diameter at different heat flux, mass flux and system pressure. Fig. 13 was obtained at a system pressure of 1 bar, mass flux of 100 kg/m^2 s and heat flux values of 39 and 65 kW/m^2. It is obvious that the nucleating bubbles had a spherical shape after departing the nucleation site and the departure diameter increased with increasing wall heat flux. For example, at wall heat flux of 39 kW/m^2, the measured bubble departure diameter was 0.182 mm, while it was 0.271 mm at a heat flux of 65 kW/m^2. An increase in heat flux leads to an increase the evaporation rate underneath and around the bubbles and thus increases bubble volume. Fig. 14 depicts the bubble departure diameter at a wall heat flux of 65 kW/m^2, system pressure of 1 bar and two mass fluxes of 100 and 200 kg/m^2 s. The shape of these bubbles was still spherical even with increasing mass flux. However, the bubble departure diameter reduced from 0.271 to 0.184 mm when the mass flux increased from 100 to 200 kg/m^2 s. Increasing mass flux leads to an increase in the inertia force, which helps “tear” these bubbles from their nucleation sites, i.e. there is less time for heat transfer from the surface or adjacent fluid and reduced growth time. Fig. 15 shows the pictures captured at different system pressures but fixed heat and mass flux. It shows that the nucleating bubbles had a smaller departure diameter with increasing system pressure, e.g. the bubble departure diameter was 0.271 mm at 1 bar, while it reduced to 0.212 mm when increasing system pressure to 2 bar. This may be attributed to the reduction in the surface tension force as the pressure increases. Surface tension force tends to hold the bubble attached at the nucleation site (on the surface). Therefore, lower surface tension force could result in reduced growth time and hence smaller bubble departure diameter.

Fig. 16 presents the effect of heat flux, mass flux and system pressure on the average bubble departure diameter. It shows that the average bubble departure diameter increased with increasing wall heat flux and decreasing mass flux and system pressure. It was also found that the average bubble departure diameter varied from 0.09 to 0.33 mm for a heat flux range of 19–84 kW/m^2 during the tested operating conditions.

3.4. Average bubble frequency

The bubble departure frequency was calculated based on the bubble growth time and the waiting time, which were measured from the bubble ebullition cycle as depicted in Fig. 17 for a selected nucleation site at 1 bar, 39 kW/m^2 and 100 kg/m^2 s. At these operating conditions, the bubble growth time was 3.5 ms, while the waiting time was only 2 ms. Therefore, the total cycle time was 5.5 ms giving a bubble frequency of 182 Hz. It was also noticed that the bubble frequency varied from one location to another. This can be seen in Fig. 18 at a system pressure of 1 bar, wall heat flux of 57 kW/m^2 and mass flux of 200 kg/m^2 s. In this figure, two nucleation sites were captured at the same heated area namely NS1 and NS2. At 0 ms, a nucleating bubble was activated at NS1, while no bubble was seen at NS2. At 3 ms, this bubble departed from the NS1 and began to slide. At 5 ms, a new nucleating bubble was captured at NS1. NS2 generated the first nucleating bubble during this sequence of images at 5 ms. After 8 ms, both these bubbles left their nucleation sites and slide on the surface. Accordingly, the bubble frequency of NS1 and NS2 was calculated to be 200 Hz (5 ms) and 125 Hz (8 ms), respectively. Although the same operating conditions and heated area were tested, the bubble frequency varied at each nucleation site. This could be either due to the different cavity size and shape (microstructures) that may result in different bubble dynamics or variation in the local wall superheat. Large cavity size can promote more contact area (between surface and fluid) leading to large bubble volume. Surface tension forces can then help hold the bubbles on the surface leading to lower generation frequency.

The effect of heat flux, mass flux and system pressure on the average bubble frequency is presented in Fig. 19. This figure shows that the average bubble frequency increased with increasing wall heat flux, mass flux and system pressure. It also depicts that, at the examined operating conditions, the average bubble frequency varied from 143 to 500 Hz when the wall heat flux changed from 19 to 84 kW/m^2. High heat flux (high wall temperature) between the surface and the growing bubble can increase the bubble generation frequency. Smaller surface tension, at high pressure, can result in a force balance that favours bubble departure, hence higher bubble generation frequency. Similarly, increasing mass flux can contribute to an earlier bubble departure and consequently higher generation frequency.

3.5. Evaluation of NSD, departure diameter and frequency models/correlations

The present experimental data were compared with existing correlations and models for calculating nucleation site density, bubble departure diameter and frequency. The mean absolute error (MAE) was used as a criterion in this evaluation as follows:

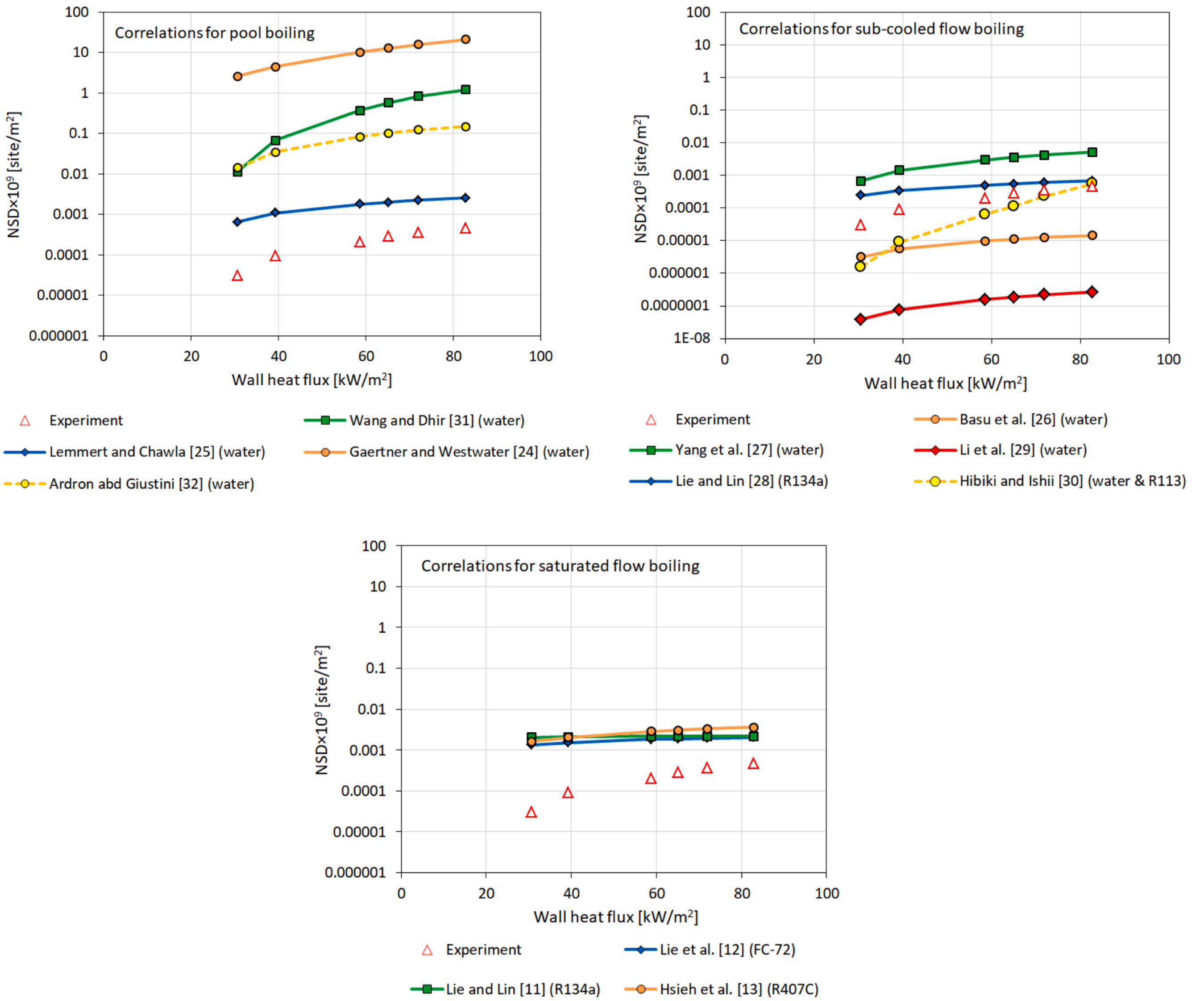

Fig. 20. Evaluation of nucleate site density at P_{sys}=1 bar and G= 100 kg/m^2 s.

$$MAE = \frac{1}{N}\sum\left|\frac{\Delta_{pred} - \Delta_{exp}}{\Delta_{exp}}\right|100\% \tag{14}$$

These models and correlations are summarised in Tables 1–3. They were proposed for pool boiling, sub-cooled flow boiling and saturated flow boiling using water and refrigerants. Fig. 20 depicts the comparison of the measured NSD with these models/correlations at a system pressure of 1 bar and mass flux of 100 kg/m^2 s. It is worth mentioning that the contact angle of the current fluid was assumed to be 10° [41] and this value was used in this comparison. The model by Hibiki and Ishii [30] included the gas constant R, which for HFE-7100 is 33.24 J/kg K. It is clear that these correlations showed the same trend as the present experiments (increasing NSD with heat flux) but with a significant deviation. This was also found when other operating conditions were assessed. This figure also shows that there is a large discrepancy among some correlations, although they were suggested for water in pool boiling or sub-cooled flow boiling e.g. Basu et al. [26] and Yang et al. [27]. It is also clear that the correlations suggested for water (hydrophobic fluid) had a larger disagreement with the present refrigerant (super-hydrophilic fluid). For example, Ardron and Giustini [32] reported that the nucleation site density strongly depended on the contact angle. They used the pool boiling data of water at a working pressure of 1–132 bar, and found that using the contact angle of vapour bubbles predicted the results well compared to the contact angle from the sessile droplet measurements. They correlated this data by introducing the Young's contact angle as a function of the surface temperature and the critical temperature, see Table 3. However, this correlation over predicted our data with a MAE more than 500 % as shown in this figure. This could be due to the large difference in fluid properties of water and HFE-7100 that could affect the value of this contact angle. It is interesting and worth mentioning that, if their procedure is adopted here using the present data in Fig. 20, the new Young's contact angle would be $\theta_Y = 0.01(T_w/T_{cr})^{-3}$. This new correlation predicted well the present data, with a MAE of 13 %. Table 5 shows the MAE for the assessment of the NSD, departure diameter and frequency correlations. It is seen that, the model by Hibiki and Ishii [30] for NSD had the smallest MAE of 62 % (at 1 bar and 100 kg/m^2 s). It is interesting to note that the comparison with Hibiki and Ishii improves with heat flux. Their model was based on experimental data for water and R113.

The correlations for the bubble departure diameter were compared with the present results as shown in Fig. 21 for a mass flux of 100 kg/m^2 s. Three of the pool boiling correlations gave the bubble departure diameter to be nearly independent of heat flux, see Fritz [15], Cole and Rohsenow [16] and Phan et al. [17]. This could be due to the fact that these correlations were proposed as a function of contact angle and fluid properties only. In contrast, the departure diameter was found to

Table 5
Evaluation of existing models and correlations.

Author(s)	P=1 [bar] MAE [%] G= 100 kg/m^2 s	P=1 [bar] MAE [%] G= 200 kg/m^2 s	P= 2 [bar] MAE [%] G= 100 kg/m^2 s	MAE [%] Average
Nucleation site density:				
Gaertner and Westwater [24]	>500	>500	>500	>500
Lemmert and Chawla [25]	>500	>500	97	>500
Wang and Dhir [31]	>500	>500	>500	>500
Ardron and Giustini [32]	>500	>500	>500	>500
Basu et al [26]	95	96	99	97
Yang et al. [27]	>500	>500	62	>500
Lie and Lin [28]	217	107	88	137
Li et al. [29]	100	100	100	100
Hibiki and Ishii [30]	62	74	100	79
Lie and Lin [11]	>500	>500	>500	>500
Lie et al. [12]	>500	>500	>500	>500
Hsieh et al. [13]	>500	>500	>500	>500
Departure diameter:				
Fritz [15]	165	273	306	248
Cole and Rohsenow [16]	88	185	52	108
Phan et al. [17]	152	252	327	244
Cole [18]	153	250	22	142
Kim and Kim [19]	340	>500	188	347
Kossolapov et al. [20]	156	91	305	184
Lie and Lin [11]	12	45	34	30
Lie et al. [12]	60	132	104	99
Hsieh et al. [13]	185	262	252	233
Generation frequency:				
Jakob and Fritz [21]	79	67	189	112
Cole [22]	43	30	61	45
Zuber [23]	56	44	104	68
Lie and Lin [11]	>500	>500	>500	>500
Lie et al. [12]	69	53	59	60
Hsieh et al. [13]	292	>500	316	415

increase with increasing heat flux as shown by Cole [18] and Kim and Kim [19]. The Jacob number introduced in these models can lead to this trend. The correlations of saturated flow boiling showed an increase in the bubble departure diameter with heat flux, which is similar to our findings. The present results were predicted well by the correlation of Lie et al. [11] with a small MAE of 12 %, while the rest of the correlations demonstrated higher disagreement, see Table 5. Kossolapov et al. [20] conducted an experimental study using sub-cooled flow boiling of water in a vertical square channel at a working pressure of 10–40 bar, mass flux of 500–1500 kg/m^2 s and inlet sub-cooling of 9.9–12.6 K. They also carried out analytical solutions to model the bubble sliding and then to predict the bubble growth time and departure diameter. In their solution, an empirical constant C_{RB} and a theoretical constant B were presented according to the range of both working pressure and mass flux. They also mentioned that the ratio between C_{RB} and B was found to be 0.5. In the present comparison, the theoretical constant was chosen from their work to be 52.1×10^{-4} m/s$^{0.5}$ at 10 bar and 500 kg/m^2 s since these were the minimum ranges reported in their study. It was found that, their solution over predicted all the present data with an average MAE of 184 %, as shown in Table 5. The high value of this constant due to high working pressure and mass flux could be the reason for this disagreement. For example, at 1 bar and 100 kg/m^2 s, if the theoretical constant was reduced from 52.1×10^{-4} m/s$^{0.5}$ to 20×10^{-4} m/s$^{0.5}$, then the mean absolute error between their solution and this data would reduce from 156 % to only 23 %. This could be considered in a similar future study.

Fig. 22 depicts the evaluation of existing correlations for calculating bubble generation frequency. All the pool boiling correlations showed

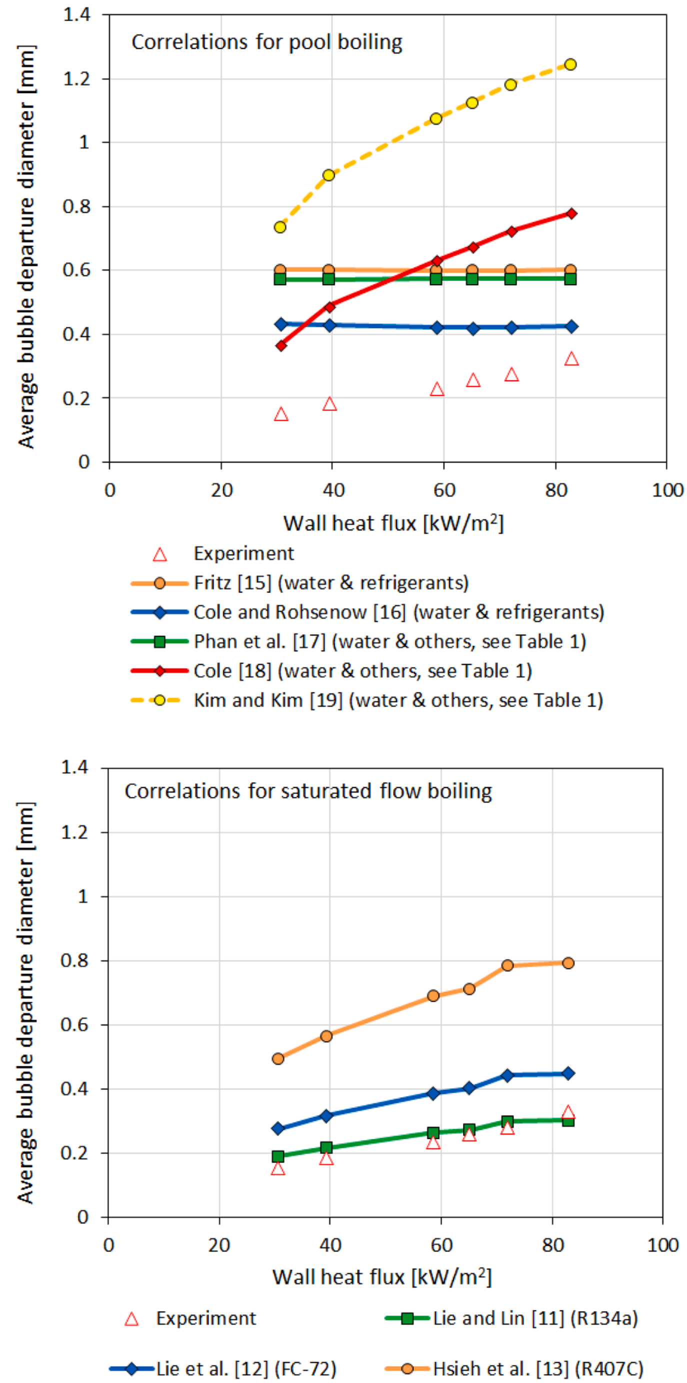

Fig. 21. Evaluation of bubble departure diameter at P_{sys}=1 bar and G=100 kg/m^2 s.

that the bubble frequency decreased with increasing heat flux, while the current results indicate an increasing trend. This could be due to the fact that re-construction of the wall thermal boundary layer in pool boiling is completely different compared to flow boiling. In pool boiling, with possible larger dry patches underneath the bubble, which increase in size with heat flux, it can take longer for the thermal boundary to re-establish, i.e. the waiting time becomes larger and thus the frequency decreases with heat flux. In flow boiling, the reformation of the wall superheated layer is faster compared to pool boiling. The correlations of saturated boiling showed the same trend as the present study but with large differences.

The disagreement between the present data and the correlations

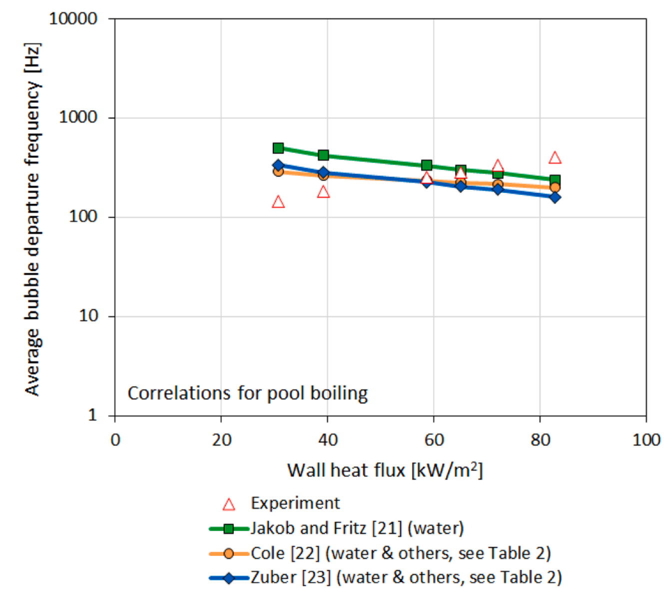

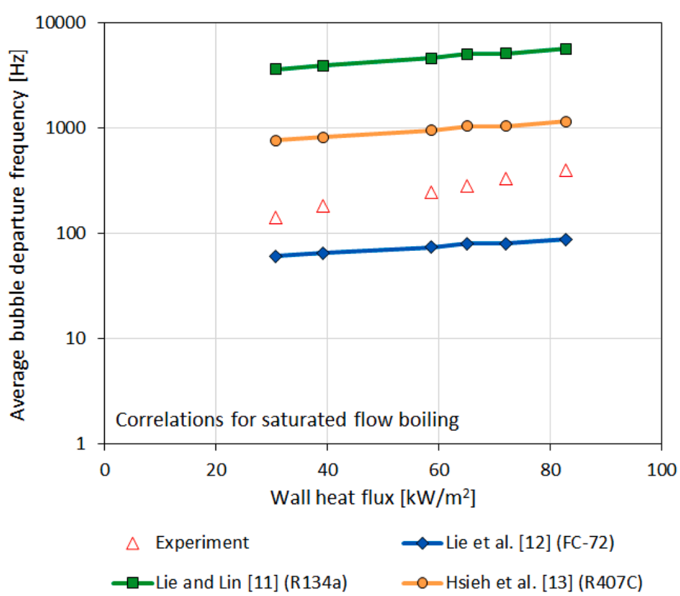

Fig. 22. Evaluation of bubble frequency at P_{sys}=1 bar and G = 100 kg/m^2 s.

could be due to the following reasons: (1) Different working fluids. For example, the surface tension of working fluids examined by these studies varies from 0.007 to 0.008 N/m at 25 °C. Water has a larger surface tension of 0.072 N/m at 25 °C compared to refrigerants. The surface tension of HFE-7100 is 0.013 N/m at 25 °C. (2) Different operating conditions. The correlations by [11,13], covered a mass flux of 200–600 kg/m^2 s at a saturation temperature of 10 and 15 °C and heat flux below 30 kW/m^2, i.e. a much higher mass flux than the present study. Lie et al. [12] produced their correlation for a mass flux of 287–431 kg/m^2 s, saturation temperature of 54 °C and heat flux below 100 kW/m^2. In the present study, the operating conditions were different, i.e. mass flux of 100–200 kg/m^2 s, saturation temperature of 61–83 °C and heat flux below 84 kW/m^2. (3) Different surface microstructures. Details on surface topography were not reported in most of these studies, and it is very likely that the surface characteristics are not similar to the surface of the present study. Different machining techniques and manufacturing settings could result in different surface microstructures even when using the same material. Surface topography should be carefully examined and reported in any heat transfer study of this nature. (4) Uncertainty in the measurement of bubble characteristics. (5) Some of the proposed correlations for calculating nucleation site density and bubble frequency were linked with the correlations of bubble departure diameter. In other words, the prediction of these two correlations is significantly affected by the accuracy of bubble diameter correlations. All these parameters could lead to different bubble characteristics that could affect the predicting capability of proposed correlations.

3.6. New proposed correlations for NSD, departure diameter and frequency

To the best of the authors' knowledge, the bubble characteristics during saturated flow boiling of this super-hydrophilic fluid (HFE-7100) were not examined in literature. Moreover, the mean absolute error of the existing correlations was found to be greater than 79 % for the NSD, greater than 30 % for departure diameter and greater than 45 % for departure frequency, see Table 5. Accordingly, new correlations were developed in the present study. Regression analysis and curve estimation methods were carried out using the Statistical Package for the Social Sciences (IBM SPSS) by evaluating our data at different control parameters. The abovementioned experimental results showed that both wall heat flux and system pressure had a significant effect on the present bubble behaviour. Therefore, these two parameters were included into the proposed new correlations.

3.7. Nucleation site density

As discussed in Section 3.2, the nucleation site density clearly increased with wall heat flux and system pressure. The effect of mass flux was insignificant as shown in Fig. 12 (a) and therefore this parameter was not included in this analysis. The new empirical correlation derived from our data is:

$$NSD = 4.3 \times 10^{-4} q_w''^{\,2.47} RP^{2.34} \tag{15}$$

The effect of system pressure was presented here as a reduced pressure RP.

3.8. Departure diameter

Section 3.3 shows that the bubble departure diameter increased with increasing wall heat flux and decreasing mass flux and system pressure. These parameters were grouped as the boiling number (heat and mass flux effect) and reduced pressure (system pressure effect). The derived empirical correlation for calculating bubble departure diameter was expressed as follows:

$$\frac{D_d}{\sqrt{\sigma/g\Delta\rho}} = 3Bo^{0.7} RP^{-0.45} \tag{16}$$

It is worth mentioning that the bubble departure diameter when using Eq. (16) is in meter. The left-side of this correlation is similar to the saturated flow boiling correlations reported in Table 1. However, the right-side differs from these correlations according to the present control dimensionless groups.

3.9. Frequency of bubble generation

As presented in Section 3.4, the present bubble frequency was found to increase with increasing wall heat flux, mass flux and system pressure. The Reynolds number takes into account the effect of inertia force. Accordingly, the experimental data points were correlated to produce a new correlation, see Eq. (17).

$$f_b = 6.5 \times 10^{-3} q_w''^{\,0.88} RP^{0.22} Re_l^{0.26} \tag{17}$$

Fig. 23 depicts the comparison between these new correlations and

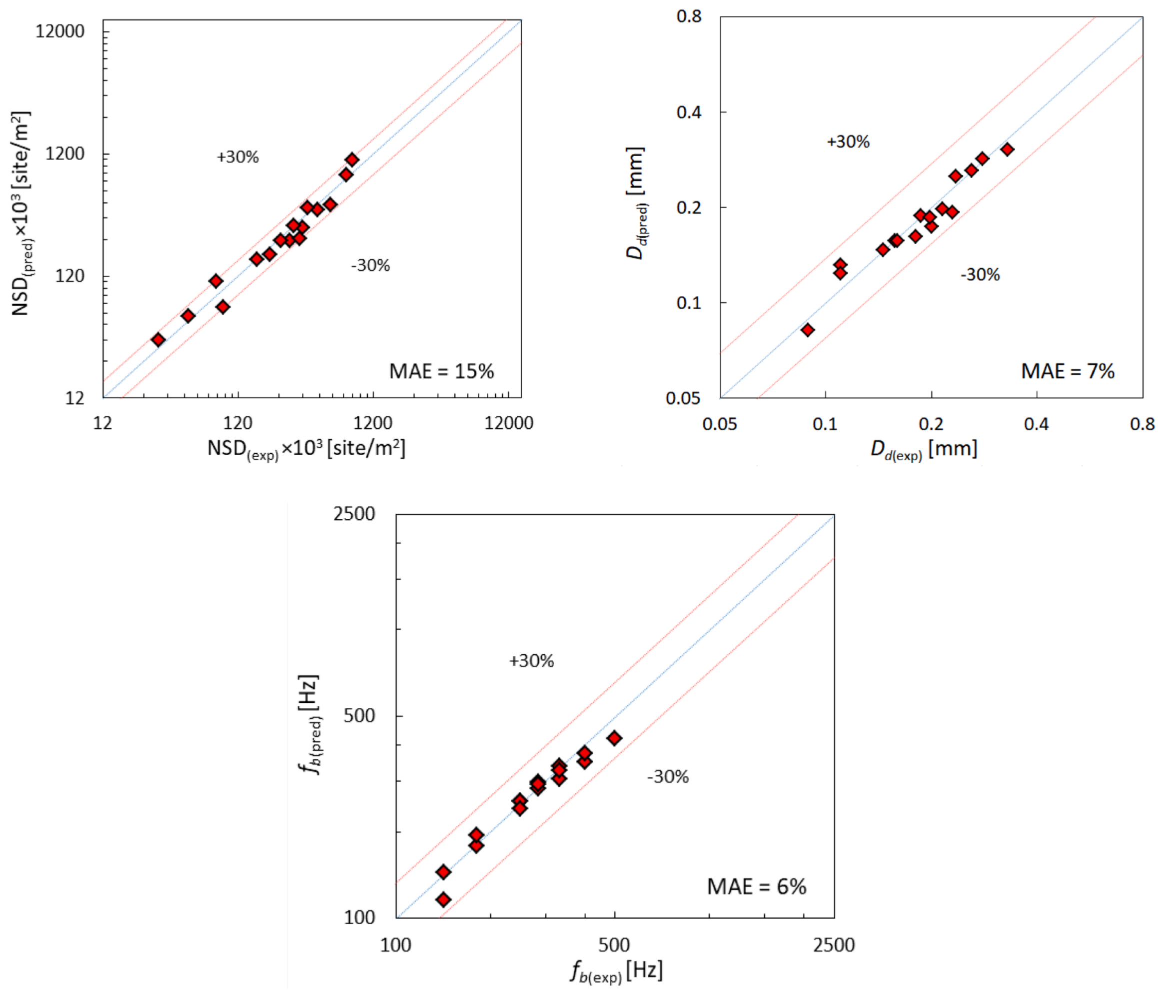

Fig. 23. Comparison of the predicted results of the proposed correlations and experimental data.

the present data. It shows that the correlations of nucleation site density, bubble departure diameter and bubble frequency predicted the experimental results with a MAE of 6–15 %. The proposed correlations covered the following saturated flow boiling conditions:

Boiling number: 1.8–6.8 $\times$ 10^{-3}
Reduced pressure: 0.045–0.09
Liquid Reynolds number: 460–954
Wall superheat: 5–17 K
Inlet sub-cooling: 5 K

Further assessment is needed to evaluate the capability of these correlations using different operating conditions and working fluids.

4. Conclusions

The present study examined the bubble dynamic characteristics of HFE-7100 in a microgap heat sink. The experiments were carried out at an inlet sub-cooling of 5 K, inlet pressure of 1 and 2 bar, mass flux of 100–200 kg/m^2 s and wall heat flux up to 84 kW/m^2. The observation area during the flow visualization studied with the high-speed, high resolution camera was 8.8 mm $\times$ 11 mm, i.e. large enough to allow capturing a significant number of active nucleation sites. The present experimental results were also compared with existing models and correlations. The following findings can be concluded from this paper:

The nucleation site density, bubble departure diameter and bubble frequency were found to increase with increasing heat flux. Increasing mass flux led to a reduction in the bubble departure diameter and an increase in the bubble frequency, while the effect on the nucleation site density was insignificant. The nucleation site density and bubble frequency increased with system pressure. However, the bubble departure diameter decreased as the pressure increased. All our tests demonstrated a strong dependence of the nucleation site density, bubble departure diameter and frequency on wall heat flux and system pressure and a weaker dependence on mass flux for the ranges studied.

Surface microstructures (number and size of surface cavities) could result in different bubble behaviour. Surface characteristics should be carefully assessed and recorded in experiments of this nature. The present study showed also that multiple-site, and not just single-side measurements, of bubble characteristics should be considered in future studies. This can provide more details of different bubble behaviour on the same heated surface.

Existing models and correlations of bubble characteristics were evaluated, and large discrepancies were found. New empirical correlations for calculating nucleation site density, bubble departure diameter and frequency were developed. These will form a valuable database for modelling research to progress since they were obtained from measurements on multiple sites. It is also recommended that further studies are needed for different ranges, fluids and substrate material and surface characteristics to compare with the equations proposed by the present study and reach general correlations

CRediT authorship contribution statement

Ali H. Al-Zaidi: Writing – review & editing, Writing – original draft, Validation, Investigation, Formal analysis. **Mohamed M. Mahmoud:**

Writing – review & editing. **Atanas Ivanov:** Investigation. **Tassos G. Karayiannis:** Writing – review & editing, Validation, Supervision, Resources, Project administration, Methodology, Investigation, Funding acquisition, Formal analysis, Conceptualization.

Declaration of competing interest

The authors declare that they have no known competing financial interests or personal relationships that could have appeared to influence the work reported in this paper.

Acknowledgements

The work was conducted with the support of the Engineering and Physical Sciences Research Council of the UK, under Grant: EP/T033045/1.

Appendix A. Uncertainty equations

General equation of absolute uncertainty, see [35]:

$$U_r = \sqrt{\left\{\frac{\partial r}{\partial X_1} U_{X1}\right\}^2 + \left\{\frac{\partial r}{\partial X_2} U_{X2}\right\}^2 + \ldots + \left\{\frac{\partial r}{\partial X_j} U_{Xj}\right\}^2}$$

where X_1, X_2 and X_j are measured parameters with uncertainties of U_{X1}, U_{X2} and U_{Xj}.

Absolute uncertainty in the average Nusselt number:

$$U_{\overline{Nu}_{exp}} = \sqrt{\left\{\frac{\partial \overline{Nu}_{exp}}{\partial \overline{h}} U_{\overline{h}}\right\}^2 + \left\{\frac{\partial \overline{Nu}_{exp}}{\partial D_h} U_{D_h}\right\}^2}$$

Absolute uncertainty in the Fanning friction factor:

$$U_{f_{exp}} = \sqrt{\left\{\frac{\partial f_{exp}}{\partial \Delta P_{meas}} U_{\Delta P_{meas}}\right\}^2 + \left\{\frac{\partial f_{exp}}{\partial D_h} U_{D_h}\right\}^2 + \left\{\frac{\partial f_{exp}}{\partial L_{ch}} U_{L_{ch}}\right\}^2 + \left\{\frac{\partial f_{exp}}{\partial G} U_G\right\}^2}$$

Absolute uncertainty in the Reynolds number:

$$U_{Re} = \sqrt{\left\{\frac{\partial Re}{\partial G} U_G\right\}^2 + \left\{\frac{\partial Re}{\partial D_h} U_{D_h}\right\}^2}$$

Absolute uncertainty in the wall heat flux:

$$U_{q''_w} = \sqrt{\left\{\frac{\partial q''_w}{\partial q''_b} U_{q''_b}\right\}^2 + \left\{\frac{\partial q''_w}{\partial H_{ch}} U_{H_{ch}}\right\}^2 + \left\{\frac{\partial q''_w}{\partial W_{ch}} U_{W_{ch}}\right\}^2}$$

Absolute uncertainty in the generation frequency:

$$U_{f_b} = \sqrt{\left\{\frac{\partial f_b}{\partial t_g} U_{t_g}\right\}^2 + \left\{\frac{\partial f_b}{\partial t_w} U_{t_w}\right\}^2}$$

Absolute uncertainty in the nucleation site density:

$$U_{NSD} = \sqrt{\left\{\frac{\partial NSD}{\partial n} U_n\right\}^2 + \left\{\frac{\partial NSD}{\partial A_c} U_{A_c}\right\}^2}$$

Data availability

Data will be made available on request.

References

[1] P. Zhou, S. Hua, C. Gao, D. Sun, R. Huang, A mechanistic model for wall heat flux partitioning based on bubble dynamics during subcooled flow boiling, Int. J. Heat Mass Transf. 174 (2021) 121295.

[2] G. Yang, W. Zhang, M. Binama, J. Sun, W. Cai, Review on bubble dynamic of subcooled flow boiling-part a: research methodologies, Int. J. Therm. Sci. 184 (2023) 108019.

[3] G. Yang, W. Zhang, M. Binama, Q. Li, W. Cai, Review on bubble dynamic of subcooled flow boiling-part b: behavior and models, Int. J. Therm. Sci. 184 (2023) 108026.

[4] J.C. Chen, A correlation for boiling heat transfer to saturated fluids in convective flow, Ind. Eng. Chem. 5 (1966) 322–329.

[5] X. Fang, F. Zhuang, C. Chen, Q. Wu, Y. Chen, Y. Chen, Y. He, Saturated flow boiling heat transfer: review and assessment of prediction methods, Heat Mass Transf. 55 (2019) 197–222.

[6] T.G. Karayiannis, M.M. Mahmoud, Flow boiling in microchannels: fundamentals and applications, Appl. Therm. Eng. 115 (2017) 1372–1397.

[7] T.G. Karayiannis and M.M. Mahmoud, "Flow boiling in micro-passages : developments in fundamental aspects and applications," in *Proceedings of the 16th International Heat Transfer Conference, IHTC-16*, 2018.

[8] A.H. Al-Zaidi, M.M. Mahmoud, T.G. Karayiannis, Flow boiling pressure drop correlation in small to micro passages, Int. J. Heat Mass Transf. 224 (2024) 125376.

[9] N. Kurul and M.Z. Podowski, "Multidimensional effects in forced convection subcooled boiling," in *Proceedings of the 9th International Heat Transfer Conference*, Jerusalem, Israel, 1990, pp. 21–25.

[10] M.M. Mahmoud, T.G. Karayiannis, Pool boiling review : part I - fundamentals of boiling and relation to surface design, Therm. Sci. Eng. Prog. 25 (2021) 101024.

[11] Y.M. Lie, T.F. Lin, Saturated flow boiling heat transfer and associated bubble characteristics of R-134a in a narrow annular duct, Int. J. Heat Mass Transf. 48 (2005) 5602–5615.

[12] Y.M. Lie, J.H. Ke, W.R. Chang, T.C. Cheng, T.F. Lin, Saturated flow boiling heat transfer and associated bubble characteristics of FC-72 on a heated micro-pin-finned silicon chip, Int. J. Heat Mass Transf. 50 (2007) 3862–3876.

[13] F.C. Hsieh, K.W. Li, Y.M. Lie, C.A. Chen, T.F. Lin, Saturated flow boiling heat transfer of R-407C and associated bubble characteristics in a narrow annular duct, Int. J. Heat Mass Transf. 51 (2008) 3763–3775.

[14] Y. Zhao, Y.C. Lin, K. Tang, M. Ishii, J.R. Buchanan-Jr, Investigation of nucleate boiling and bubble dynamics at multiple nucleation sites in subcooled boiling flow, Int. J. Heat Mass Transf. 219 (2024) 124886.
[15] W. Fritz, Berech des maximal volume von dampf blasen, Phys. Z. 36 (1935) 379–388.
[16] W.M.R.R. Cole, Correlation of bubble departure diameters for boiling of saturated liquids, Chem. Eng. Prog. Symp. Ser. 65 (1969) 211–213.
[17] H.T. Phan, N. Caney, P. Marty, S. Colasson, J. Gavillet, A model to predict the effect of contact angle on the bubble departure diameter during heterogeneous boiling, Int. Commun. Heat Mass Transf. 37 (8) (2010) 964–969.
[18] R. Cole, Bubble frequencies and departure volumes at subatmospheric pressures, AIChE J. 13 (4) (1967) 779–783.
[19] J. Kim, M.H. Kim, On the departure behaviors of bubble at nucleate pool boiling, Int. J. Multiph. Flow 32 (10–11) (2006) 1269–1286.
[20] A. Kossolapov, M.T. Hughes, B. Phillips, M. Bucci, Bubble departure and sliding in high-pressure flow boiling of water, J. Fluid Mech. 987 (2024).
[21] W. Jakob, M. Fritz, "Versuche über den verdampfungsvorgang. Forschung auf dem Gebiet des Ingenieurwesens A," vol. 2, no. 12, pp. 345–447, 1931.
[22] R. Cole, A photographic study of pool boiling in the region of the critical heat flux, AIChE J. 6 (4) (1960) 533–538.
[23] N. Zuber, Nucleate boiling: the region of isolated bubbles similarly with natural convection, Int. J. Heat Mass Transf. 6 (1963) 53–65.
[24] W.J. Gaertner RF, Population of active sites in nucleate boiling heat transfer, Chem. Eng. Prog. Symp. Ser. 56 (1960) 39–48.
[25] M. Lemmert, L.M. Chawla, Influence of flow velocity on surface boiling heat transfer coefficient, Heat Transf. Boil. 237 (247) (1977).
[26] N. Basu, G.R. Warrier, V.K. Dhir, Onset of nucleate boiling and active nucleation site density during subcooled flow boiling, J. Heat Transf. 124 (2002) 717–728.
[27] L.X. Yang, A. Guo, D. Liu, Experimental investigation of subcooled vertical upward flow boiling in a narrow rectangular channel, Exp. Heat Transf. 29 (2) (2016) 221–243.
[28] Y.M. Lie, T.F. Lin, Subcooled flow boiling heat transfer and associated bubble characteristics of R-134a in a narrow annular duct, Int. J. Heat Mass Transf. 49 (13–14) (2006) 2077–2089.
[29] Q. Li, J. Yongjun, A. Maria, C. Ping, Y. Junchong, C. Jie, H. Jason, Development, verification and application of a new model for active nucleation site density in boiling systems, Nucl. Eng. Des. 328 (2018) 1–9.
[30] T. Hibiki, M. Ishii, Active nucleation site density in boiling systems, Int. J. Heat Mass Transf. 46 (14) (2003) 2587–2601.
[31] C.H. Wang, V.K. Dhir, Effect of surface wettability on active nucleation site density during pool boiling of water on a vertical surface, J. Heat Transf. 115 (3) (1993) 659–669.
[32] K.H. Ardron, G. Giustini, On the wetting behavior of surfaces in boiling, Phys. Fluids 33 (11) (2021).
[33] A.H. Al-Zaidi, M.M. Mahmoud, T.G. Karayiannis, Flow boiling of HFE-7100 in microchannels: experimental study and comparison with correlations, Int. J. Heat Mass Transf. 140 (2019) 100–128.
[34] ISO-4288, "Geometrical product specifications (GPS) – Surface texture: profile method – rules and procedures for the assessment of surface texture," 1996.
[35] H.W. Coleman and W.G. Steele, *Experimentation and Uncertainty Analysis For Engineers*, 3nd ed. New York: Wiley, Chichester, 2009.
[36] T. Ren, Z. Zhu, M. Yan, J. Shi, C. Yan, Experimental study on bubble nucleation and departure for subcooled flow boiling in a narrow rectangular channel, Int. J. Heat Mass Transf. 144 (2019) 118670.
[37] D. Copeland, Optimization of parallel plate heatsinks for forced convection, Sixt. Annu. IEEE Semicond. Therm. Meas. Manag. Symp. IEEE (2000) 266–272.
[38] P.X. Jiang, M.H. Fan, G.S. Si, Z.P. Ren, Thermal hydraulic performance of small scale micro-channel and porous-media heat exchangers, Int. J. Heat Mass Transf. 44 (2001) 1039–1051.
[39] P.S. Lee, S.V. Garimella, Thermally developing flow and heat transfer in rectangular microchannels of different aspect ratios, Int. J. Heat Mass Transf. 49 (17–18) (2006) 3060–3067.
[40] Y.Y. Hsu, On the size range of active nucleation cavities on a heating surface, J. Heat Transf. 84 (1962) 207–215.
[41] V. Grishaev, A. Amirfazli, S. Chikov, Y. Lyulin, O. Kabov, Study of edge effect to stop liquid spillage for microgravity application, Microgr. Sci. Technol. 25 (1) (2013) 27–33.